ΕΘΝΙΚΟ ΜΕΤΣΟΒΙΟ ΠΟΛΥΤΕΧΝΕΙΟ
ΣΧΟΛΗ ΕΦΑΡΜΟΣΜΕΝΩΝ ΜΑΘΗΜΑΤΙΚΩΝ & ΦΥΣΙΚΩΝ ΕΠΙΣΤΗΜΩΝ
ΤΟΜΕΑΣ ΦΥΣΙΚΗΣ
ΕΡΓΑΣΤΗΡΙΟ ΠΕΙΡΑΜΑΤΙΚΗΣ ΦΥΣΙΚΗΣ ΥΨΗΛΩΝ ΕΝΕΡΓΕΙΩΝ & ΣΥΝΑΦΟΥΣ ΟΡΓΑΝΟΛΟΓΙΑΣ

ΕΘΝΙΚΟ ΚΕΝΤΡΟ ΕΡΕΥΝΑΣ ΦΥΣΙΚΩΝ ΕΠΙΣΤΗΜΩΝ «ΔΗΜΟΚΡΙΤΟΣ»
ΙΝΣΤΙΤΟΥΤΟ ΝΑΝΟΕΠΙΣΤΗΜΗΣ & ΝΑΝΟΤΕΧΝΟΛΟΓΙΑΣ
ΙΝΣΤΙΤΟΥΤΟ ΠΥΡΗΝΙΚΗΣ & ΣΩΜΑΤΙΔΙΑΚΗΣ ΦΥΣΙΚΗΣ

ΔΙΑΤΜΗΜΑΤΙΚΟ ΠΡΟΓΡΑΜΜΑ ΜΕΤΑΠΤΥΧΙΑΚΩΝ ΣΠΟΥΔΩΝ
ΦΥΣΙΚΗ & ΤΕΧΝΟΛΟΓΙΚΕΣ ΕΦΑΡΜΟΓΕΣ

ΤΟΜΕΑΣ ΦΥΣΙΚΗΣ
ΕΡΓΑΣΤΗΡΙΟ ΠΕΙΡΑΜΑΤΙΚΗΣ ΦΥΣΙΚΗΣ ΥΨΗΛΩΝ ΕΝΕΡΓΕΙΩΝ
& ΣΥΝΑΦΟΥΣ ΟΡΓΑΝΟΛΟΓΙΑΣ

Ανάπτυξη του συστήματος αυτομάτου ελέγχου του New Small Wheel του πειράματος ATLAS
και
μελέτη ανιχνευτών MicroMegas σε περιβάλλον υψηλής ακτινοβολίας

ΜΕΤΑΠΤΥΧΙΑΚΗ ΕΡΓΑΣΙΑ
ΤΟΥ

Νικόλαου Δ. Κανέλλου

Επιβλέπων:
Θεόδωρος Αλεξόπουλος
Καθηγητής Ε.Μ.Π.

ΑΘΗΝΑ
Σεπτέμβριος 2023

Εθνικο Μετσοβιο Πολυτεχνειο
Σχολη Εφαρμοσμενων Μαθηματικων & Φυσικων Επιστημων
Τομεας Φυσικης
Εργαστηριο Πειραματικης Φυσικης Υψηλων Ενεργειων & Συναφους Οργανολογιας

Εθνικο Κεντρο Ερευνας Φυσικων Επιστημων «Δημοκριτος»
Ινστιτουτο Νανοεπιστημης & Νανοτεχνολογιας
Ινστιτουτο Πυρηνικης & Σωματιδιακης Φυσικης

Ανάπτυξη του συστήματος αυτομάτου ελέγχου του New Small Wheel του πειράματος ATLAS
και
μελέτη ανιχνευτών MicroMegas σε περιβάλλον υψηλής ακτινοβολίας

ΜΕΤΑΠΤΥΧΙΑΚΗ ΕΡΓΑΣΙΑ

του

Νικόλαου Δ. Κανέλλου

Επιβλέπων: Θεόδωρος Αλεξόπουλος
Καθηγητής Ε.Μ.Π.

Εγκρίθηκε από την τριμελή εξεταστική επιτροπή τον Σεπτέμβριο 2023.

.....	.....	.....
Θ. Αλεξόπουλος	Ε. Γαζής	Σ. Μαλτέζος
Καθηγητής Ε.Μ.Π.	Ομ. Καθηγητής Ε.Μ.Π.	Ομ. Καθηγητής Ε.Μ.Π.

Αθήνα, Σεπτέμβριος 2023

.....
Νικόλαος Δ. Κανέλλος
Φυσικός Εφαρμογών Ε.Μ.Π.

NATIONAL TECHNICAL UNIVERSITY
OF ATHENS
SCHOOL OF APPLIED MATHEMATICS &
PHYSICAL SCIENCES
DEPARTMENT OF PHYSICS
LABORATORY OF EXPERIMENTAL
HIGH ENERGY PHYSICS & RELATED
TECHNOLOGY-INSTRUMENTATION

NATIONAL CENTER FOR SCIENTIFIC
RESEARCH "DEMOCRITOS"
INSTITUTE OF NANOSCIENCE & NAN-
OTECHNOLOGY
INSTITUTE OF NUCLEAR & PARTICLE
PHYSICS

INTERDISCIPLINARY INTERDEPARTMENTAL POSTGRADUATE PROGRAM
PHYSICS & TECHNOLOGICAL APPLICATIONS

DEPARTMENT OF PHYSICS
LABORATORY OF EXPERIMENTAL HIGH ENERGY PHYSICS
& RELATED TECHNOLOGY-INSTRUMENTATION

Development of detector control system of New Small Wheel in ATLAS experiment and study of MicroMegas detectors in high radiation environment

MASTER THESIS
OF

Nikolaos D. Kanellos

Supervisor:
Theodoros Alexopoulos
Professor, N.T.U.A

ATHENS
September 2023

NATIONAL TECHNICAL UNIVERSITY OF ATHENS
SCHOOL OF APPLIED MATHEMATICS & PHYSICAL SCIENCES
DEPARTMENT OF PHYSICS
LABORATORY OF EXPERIMENTAL HIGH ENERGY PHYSICS & RELATED TECHNOLOGY-INSTRUMENTATION

NATIONAL CENTER FOR SCIENTIFIC RESEARCH "DEMOCRITOS"
INSTITUTE OF NANOSCIENCE & NANOTECHNOLOGY
INSTITUTE OF NUCLEAR & PARTICLE PHYSICS

Development of detector control system of New Small Wheel in ATLAS experiment and study of MicroMegas detectors in high radiation environment

MASTER THESIS

of

Nikolaos D. Kanellos

Supervisor: Theodoros Alexopoulos
Professor, N.T.U.A

Exam committee.

T. Alexopoulos Professor, N.T.U.A	E. Gazis Emeritus Professor, N.T.U.A	S. Maltezos Emeritus Professor, N.T.U.A

Athens, September 2023

.....
Nikolaos D. Kanellos
Applied Physicist N.T.U.A

Περιληψη

Μετά από μια μακρά περίοδο έρευνας και ανάπτυξης, περί τα τέλη Νοεμβρίου του 2021, οι νέοι μικροί τροχοί (New Small Wheel) εγκαταστάθηκαν επιτυχώς, στο πείραμα ATLAS, σηματοδοτώντας μια από τις πιο σημαντικές αναβαθμίσεις κατά την δεύτερη περίοδο μακράς διακοπής λειτουργίας (long shutdown 2). Οι νέοι μικροί τροχοί, φέρουν δύο νέες ανιχνευτικές τεχνολογίες, τους Micromegas και small-strip Thin Gap Chambers, οι οποίες είναι ειδικά σχεδιασμένες για τις νέες συνθήκες που θα επιβάλλει ο υψηλής φωτεινότητας μεγάλος αδρονικός επιταχυντής (high-luminosity Large Hadron Collider). Ο HL-LHC αποτελεί την αρχή μιας νέας εποχής στην αναζήτηση νέων φαινομένων φυσικής καθώς και στην πιο λεπτομερή μελέτη των ήδη γνωστών. Αυτό θα επιτευχθεί με την αύξηση της φωτεινότητας η οποία συνεπάγεται την αύξηση των παραγόμενων δεδομένων. Η παρούσα διπλωματική εργασία πραγματεύεται την ανάπτυξη και συντήρηση του συστήματος αυτομάτου ελέγχου των νέων μικρών τροχών (NSW), καθώς και την μελέτη των ανιχνευτών Micromegas σε περιβάλλον υψηλής ακτινοβολίας.

Η εργασία χωρίζεται σε τρία μέρη. Στο πρώτο μέρος γίνεται μια γενική εισαγωγή για το ευρωπαϊκό κέντρο πυρηνικών ερευνών (CERN), το σύμπλεγμα των επιταχυντών του, καθώς και τα κύρια πειράματα από τα οποία αποτελείται. Στην συνέχεια, έμφαση δίνεται στο πείραμα ATLAS, επεξηγώντας τα κύρια ανιχνευτικά του συστήματα, το σύστημα σκανδαλισμού και λήψης δεδομένων καθώς στο σύστημα αυτομάτου ελέγχου (κεφάλαιο 1). Επιπρόσθετα, γίνεται αναφορά στην προετοιμασία του πειράματος ATLAS για την νέα εποχή υψηλής φωτεινότητας του μεγάλου αδρονικού επιταχυντή. Δίνοντας έμφαση στην αναγκαιότητα αντικατάστασης των μικρών τροχών και την δομή νέων μικρών τροχών που θα τους αντικαταστήσουν (κεφάλαιο 2). Το πρώτο μέρος ολοκληρώνεται με την επεξήγηση των ανιχνευτικών τεχνολογιών που θα φέρουν οι νέοι μικροί τροχοί καθώς και των ηλεκτρονικών που θα χρησιμοποιηθούν για το σύστημα σκανδαλισμού και συλλογής δεδομένων (κεφάλαιο 3).

Στο δεύτερο μέρος, γίνεται αναφορά στο σύστημα αυτομάτου ελέγχου, κάνοντας μια γενική εισαγωγή για τον σκοπό του, τον τρόπο που έχει σχεδιαστεί, το πρόγραμμα που χρησιμοποιείται για την ανάπτυξη του και τέλος τα γραφικά περιβάλλοντα που χρησιμοποιούνται για τον χειρισμό του (κεφάλαιο 4). Στην συνέχεια, η περιγραφή συγκεκριμενοποιείται στο σύστημα αυτομάτου ελέγχου των νέων μικρών τροχών, αναφέροντας την αρχιτεκτονική, τα δομικά του μέρη καθώς και την συνεισφορά που έγινε στα πλαίσια αυτής της διπλωματικής εργασίας (κεφάλαιο 5).

Στο τρίτο μέρος διατυπώνονται οι θεμελιώδης αρχές της αλληλεπίδρασης των σωματιδίων με την ύλη, δίνοντας έμφαση στην περίπτωση των ανιχνευτών αερίου (κεφάλαιο 6). Το τρίτο μέρος ολοκληρώνεται με την μελέτη των ανιχνευτών Micromegas σε περιβάλλον υψηλής ακτινοβολίας. Πιο συγκεκριμένα, επεξηγείται η εγκατάσταση στην οποία οι μελέτες έλαβαν μέρος, η πειραματική διάταξη που μελετήθηκε και τέλος τα αποτελέσματα που εξήχθησαν (κεφάλαιο 7).

Abstract

After a long period of research and development, in late November 2021, the New Small Wheels (NSW) were successfully installed in the cavern of ATLAS experiment, marking the completion of one of the most significant upgrades during Long Shutdown 2. The NSW introduces two new detector technologies, Micromegas and small-strip Thin Gap Chambers, specifically designed to operate under the new conditions imposed by the high-luminosity Large Hadron Collider. The HL-LHC is the beginning of a new era in the search of new physics phenomena and the detailed study of already known ones by increasing luminosity, resulting in more data. This master's thesis presents the development and maintenance of the NSW detector control system, as well as the study of Micromegas detectors in high-radiation environment.

The thesis is divided into three parts. In the first part, a general introduction is provided about the European Organization for Nuclear Research (CERN), its accelerator complex and the main experiments it comprises of. Subsequently, emphasis is given on the ATLAS experiment, with a description of its main sub-detector systems, the data acquisition and trigger system, as well as the detector control system (Chapter 1). Additionally, there is a reference to the preparation of the ATLAS experiment for the new era of high luminosity LHC, focusing on the necessity to replace the small wheels and on the structure of the NSW that will replace them (Chapter 2). The first part ends with a description of the new detector technologies that will be introduced by the NSW and the electronics used for the trigger and data acquisition system (Chapter 3).

In the second part, there is a reference to the detector control system, providing a general introduction to its purpose, the program used for its development, and the graphical environments used for its operation (Chapter 4). Furthermore, the description of the NSW detector control system is detailed, including its architecture, structural parts, and the contributions made within the scope of this thesis (Chapter 5).

In the third part, the fundamental principles of particle interaction with matter are analysed, emphasising on the case of gas detectors (Chapter 6). In addition, a reference to the study of Micromegas detectors in a high-radiation environment follows. Focusing on the experimental setup, the parameters that were studied and the results that were obtained (Chapter 7).

Acknowledgments

It has been over a year since the beginning of this beautiful journey and I feel compelled to start by thanking the man who believed in me and gave me the opportunity to work with him and his team in ATLAS experiment, Theodoros Alexopoulos. I would also like to thank Polyneikis Tzanis and Christos Paraskevopoulos for the guidance and the assistance they provided throughout the course of my master's thesis in the field of DCS. Concerning the second part of my thesis, I would like to thank Chara Kitsaki who generously shared her code and experience in the field of detector analysis. Ferthermore, I would like to express my thanks to Efstathios Karentzos and Ioannis Drivas-Koulouris for their guidance and their constant willingness to help. Last but certainly don't least, I am deeply grateful to my family, my friends and my partner for their constant support and encouragement in good and bad times.

Contents

List of Figures

Part I

ATLAS experiment at CERN

I Introduction

1.1 CERN

The European Organization for Nuclear Research, known as CERN, is an intergovernmental organization, established in 1954. It is located on the France–Switzerland border, in a northwestern suburb of Geneva and is the largest particle physics laboratory in the world. Its mission is to uncover what the universe is made of and how it works. It achieves this by providing a unique range of particle accelerator facilities and detectors to researchers.

The main parts of CERN's facilities are the Large Hadron Collider (LHC) as well as the four experiments, ATLAS, Compact Muon Solenoid (CMS), A Large Ion Collider Experiment (ALICE) and Large Hadron Collider beauty (LHCb).

ATLAS is a general-purpose particle physics experiment which has contributed to the discovery of Higgs boson, in the studies of CP symmetry violation and generally in a range of physics topics. CMS is also a general-purpose particle physics experiment contributing to the same physics topics using different operating principle. ALICE experiment has been designed for studying heavy ion collisions. Studying the physics of strongly interacting matter at extreme energy densities, gives the opportunity to researchers to study the phase of matter called quark-gluon plasma. LHCb experiment focuses in the studies of bottom quark and therefore in the study of CP violation[1].

1.2 Accelerators complex

The journey of particles begins from a bottle of negative hydrogen ions (H^-), which are accelerated into a linear accelerator called LINAC-4 [2]. The LINAC accelerates the H^- to an operating energy of 160 MeV and injectes them to Proton Synchrotron Booster (PSB), while they are stripped of their two electrons to leave only protons. PSB is the first and smallest circular accelerator which accelerates protons up to 2 GeV and feeds them into Proton Synchrotron (PS). PS has an important role in CERN's accelerator complex since it accelerates either protons from PSB or heavy ions from Low Energy Ion Ring (LEIR) up to 26 GeV. After that, the protons are injected into Super Proton Synchrotron (SPS), a 7 km circular accelerator, where they reach the energy of 450 GeV and are finally transferred to the two beam pipes of the LHC, where they reach the energy of 6.5 TeV [3]. In the next figure, we see a schematic representation of the accelerators complex of CERN along with each experiment.

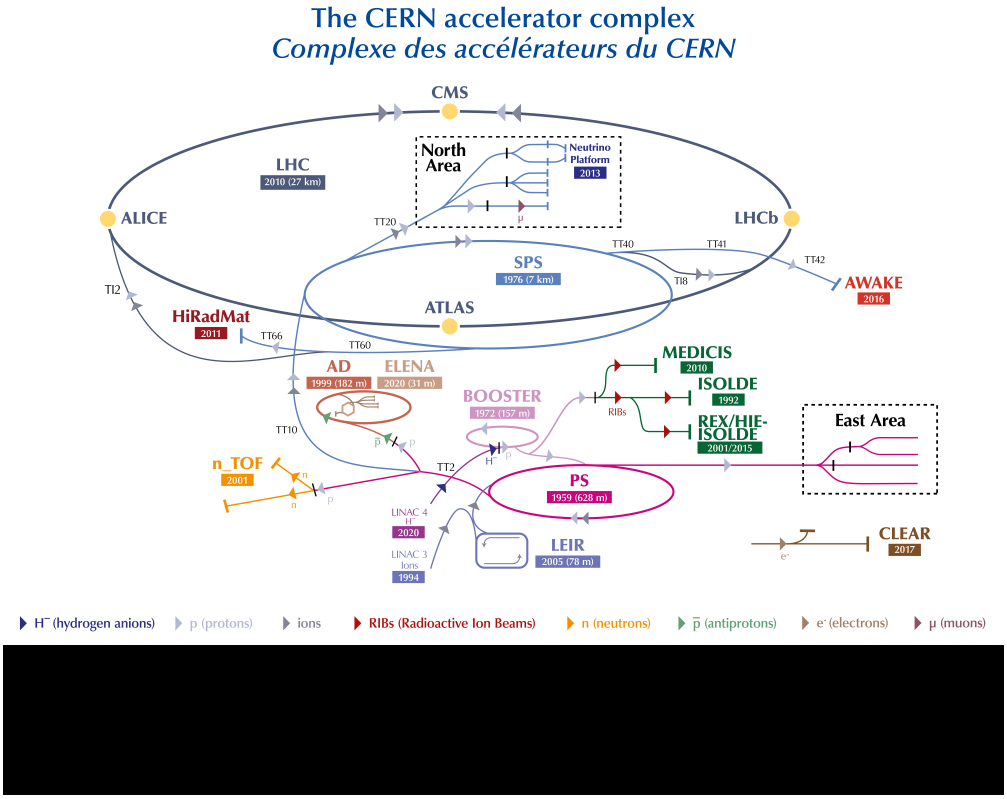

Figure 1.1: CERN's accelerator complex.

1.3 Large Hadron Collider (LHC)

LHC is the biggest and most powerful circular accelerator ever build. Its circumference is nearly 27 km and its distance from the surface of earth varies from 50 m to 175 m. It consists of two pipes (1.2) in which particles move in bunches, in opposite directions and are brought into collisions inside four detectors-experiments. The total energy at each collision point (center of mass) is equal to 13 TeV.

Its basic structural parts are the dipole magnets, the quadrupole magnets and the multipole magnets. Dipole magnets are used to bend particles trajectories and keep them in circular orbit. Quadrupole magnets are used to focus and defocus the beams and finally multipole magnets performe several corrections to the beams [4].

With particles accelerated to nearly the speed of light and colliding at such high energies, the LHC provides researchers with the opportunity to experimentally examine existing theories and gather clues for the development of new ones.

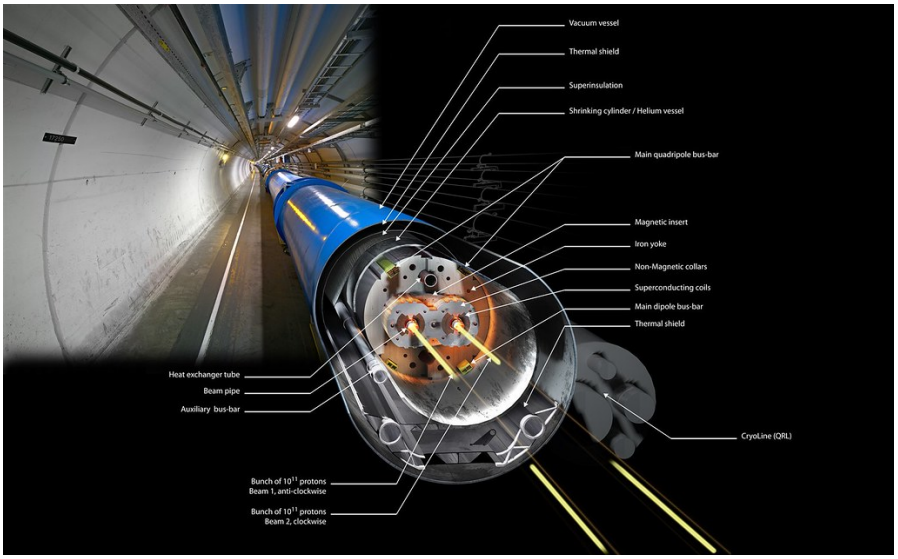

Figure 1.2: Dipole magnet.

1.3.1 LHC performance

In high energy experiments, particles energy is of great importance since it imposes an upper limit of (collision) products mass. The higher the energy of the collided particles the higher the mass of collision's products. Another equally important parameter is the number of "useful" interactions (number of events). The parameter that quantifies the ability of an accelerator to produce adequate number of events is, *luminosity* [5]. Luminosity is defined as the ratio of the number of detected events in a certain period of time to the cross section.

$$\mathcal{L} = \frac{1}{\sigma}\frac{\mathrm{d}N}{\mathrm{d}t} \tag{1.1}$$

and it has dimensions of events per time per area, $\mathrm{cm}^{-2}\mathrm{s}^{-1}$. Therefore, scientists aim to the highest possible luminosity.

1.4 ATLAS experiment

ATLAS is one of the biggest detectors of LHC that contributes on general-purpose particle physics research [6]. It has been designed to detect the widest possible range of signals so that it is able to detect any new physical process or any new particle formed. It has a cylindrical shape (1.3) with a total length of 44 m, it is 25 m in diameter and weights about 7000 t.

Its main parts are, (i) the Inner Detector (ID) which contributes in pattern recognition, momentum resolution and both primary and secondary vertex measurements for charged tracks, (ii) the magnet system which bends the trajectories of charged particles, (iii) the calorimeters which are responsible for precision measurements, jet reconstruction and energy measurements, (iv) the muon spectrometer

which contributes in momentum tracking and triggering and (v) the trigger, data acquisition (TDAQ) and DCS.

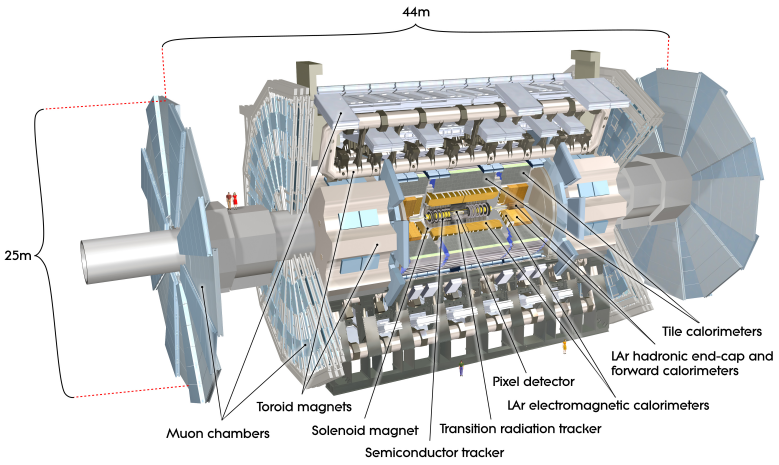

Figure 1.3: Schematic representation of ATLAS detector.

Pseudorapidity

In experimental particle physics, pseudorapidity, η, is a commonly used spatial coordinate describing the angle of a particle relative to the beam axis.

$$\eta \equiv -\ln\left[\tan\frac{\theta}{2}\right] \tag{1.2}$$

where θ is is the angle between the particle three-momentum and the positive direction of the beam axis. In the following figure we can observe some pseudorapidity values in different θ angles.

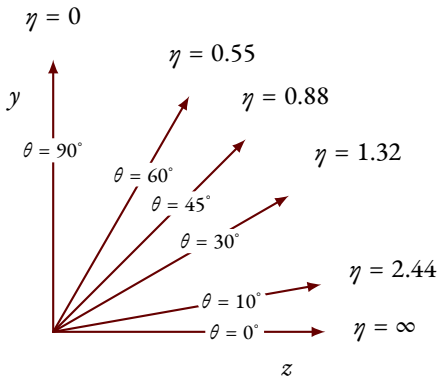

Figure 1.4: Pseudorapidity values shown on a polar plot.

1.4.1 Inner Detector

The ID is the closest system to beamline pipe, located just 3.3 cm away from it. As we can see in the figure 1.5a, it is 6.2 m long and its diameter is 2.1 m. The ID, contributes to the measurement of direction, momentum and charge of electrically-charged particles and its main components are, (i) Pixel Detector (ii) Semiconductor Tracker (SCT) and (iii) Transition Radiation Tracker (TRT) [7].

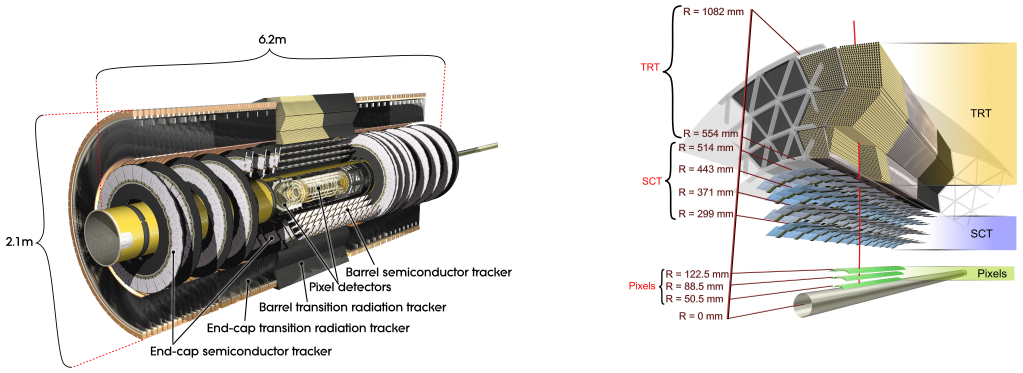

(a) Cut-away view of ID. (b) ID subsystems

Figure 1.5: ATLAS Inner Detector (ID).

Pixel Detector is the most inner part of ID. It consists of four concentric barrels of silicon pixels, three disks on each side of the end-cap which complete the angular coverage and it contributes to the tracking of charged particles.

SCT surrounds the Pixel Detector and it has the same operational principle but differs in structure since it is made of "micro-strips" of silicon sensors contributing in reconstruction of particle tracks. The two sub-detectors cover the region of $|\eta| < 2.5$.

TRT is the final layer of ID. In contrast to the other two technologies, it is made of thin-walled drift tubes ("straws"), each one of which has a diameter of 4 mm with a 30 μm gold-plated tungsten wire in its centre. The straws are filled with a gas mixture. As charged particles cross through the straws, they ionise[1] the gas creating a detectable electric signal which is used to reconstruct their tracks.

1.4.2 Magnet system

ATLAS experiment consists of four magnetic sub-systems, the Central Solenoid, the Barrel Toroid and two End-cap Toroid. All sub-systems are superconducting, cooled at about 4.5 K in order to provide the necessary strong magnetic fields [8].

[1] Ionization is the process by which an atom or a molecule acquires a negative or positive charge by gaining or losing electrons. In our case we refer always to the loss of electrons.

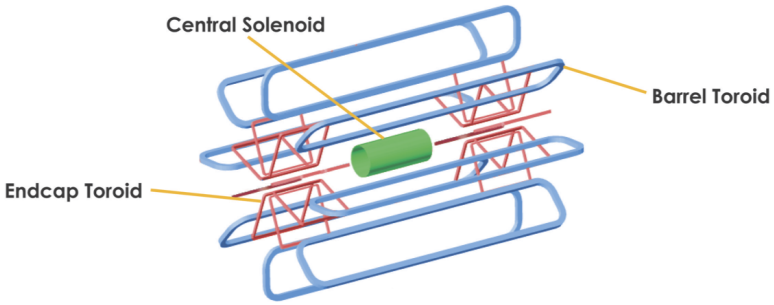

Figure 1.6: Schematic representation of ATLAS magnets.

The Central Solenoid is 5.6 m long, 2.56 m in diameter and weights over 5 t. It surrounds the inner detector, providing a 2 T magnetic field which bends particles trajectories for momentum measurements.

The Toroid magnets (Barrel and End-cap) are composed of eight coils each one of which is housed in its own cryostat and generate a toroidal magnetic field of 4 T which is almost perpendicular to the track of particles allowing the measurements of muons momentum. The Barrel Toroid has a length of 25.3 m and weights about 830 t while the End-cap Toroids have 5 m axial length and 10.7 m outer diameter.

1.4.3 Calorimeters

Calorimeters surround the ID and are designed to absorb most of the products of collisions, measuring their energy and contributing to particles' reconstruction. They consist of two components, the Liquid Argon (LAr) Calorimeter [9] and the Tile Hadronic Calorimeter [10].

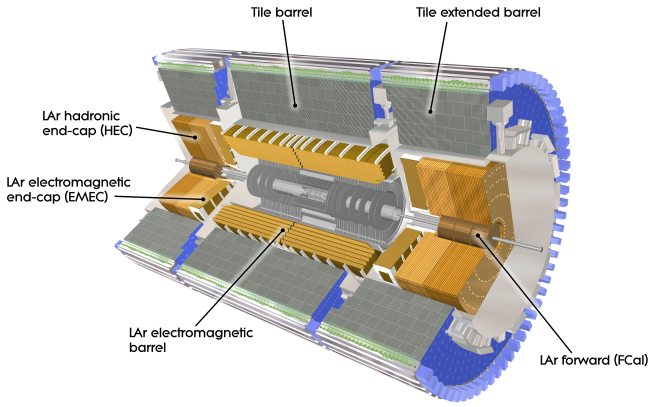

Figure 1.7: Schematic representation of calorimeterrs.

The LAr Calorimeter surrounds the ID and comprises of four sub-detectors, Electromagnetic Barrel (EMB), Electromagnetic End-Cap (EMEC), Hadronic End-Cap (HEC) and forward calorimeters. They are made of metal (either tungsten, copper or lead) and they are filled with liquid argon[2] as an active material . Their operation is based on absorbing incoming particles that are converted into a "shower" of new, lower energy particles.

Tile calorimeters surrounds the LAr Calorimeter and measures the energy of hadronic particles. They are made of iron plates as absorber and plastic scintillating tiles as the active material. Both technologies have been designed for trigger as well as for precision measurements of electrons, photons, jets, and missing transverse energy (E_T).

1.4.4 Muon spectrometer

The muon spectrometer contributes in detection, measurement and trigger of muons[3] that pass through ID and Calorimeters undetected. Its operation is based on the magnetic deflection of muons that is being provided from the three (air-core) toroid magnets. It consisted of four sub-systems, (i) MDT (ii) CSC (iii) RPC and (iv) TGC [11].

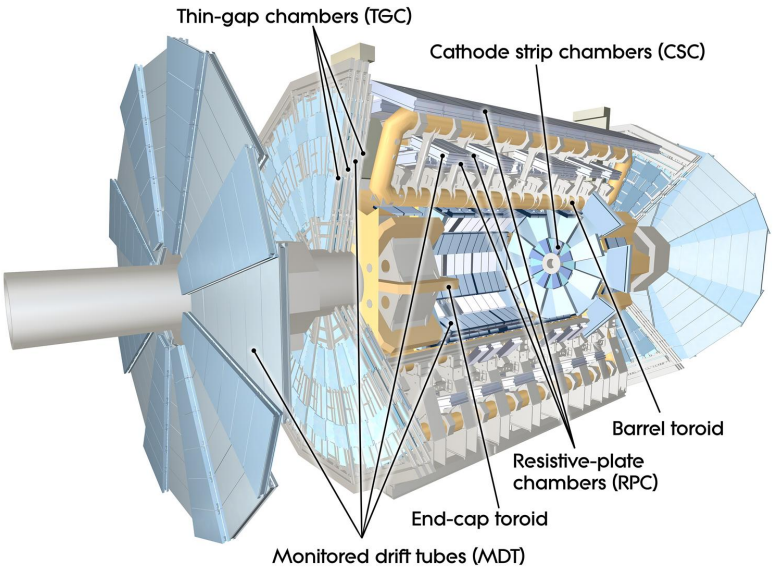

Figure 1.8: Schematic representation of muon spectrometer.

The first two detector technologies contribute to precision measurements, while the other two contribute to trigger mechanism. In the barrel region, tracks are measured in chambers and are arranged in three cylindrical layers around the beam axis, while in transition and end-cap region chambers are installed vertically.

[2] due to its inherent linear energy response and radiation tolerance.
[3] Muons are elementary particles similar to electron but with much greater mass

Within a significant portion of the pseudorapidity range, the MDTs offer precise measurements of track coordinates in the primary, bending, direction of the magnetic field. In large pseudorapidity values and close to interaction point, CSCs with higher granularity are used to sustain the demanding rate as well as the background conditions. For the trigger system, RPCs are used in the barrel while TGCs are used in the end-cap region.

Monitored Drift Tubes (MDT)

The MDT chambers consist of 3-4 layers (precision) aluminium drift tubes, each one of which has approximately 30 mm outer diameter, 400 μm wall thickness and a W−Re wire of 50 μm diameter in the centre. (1.9a). They operate with an Ar:CO_2 gas mixture at 3 bar pressure. Their operation principle is based on ionisation of gas and the collection of resulting electrons by the tungsten-rhenium wire which is under a potential of 3080 V. MDTs cover almost all the pseudorapidity region, $|\eta| < 2.7$ and they have a spatial resolution of 80 μm for a single tube which can minimised around 40 to 50 μm for a multi-layer.

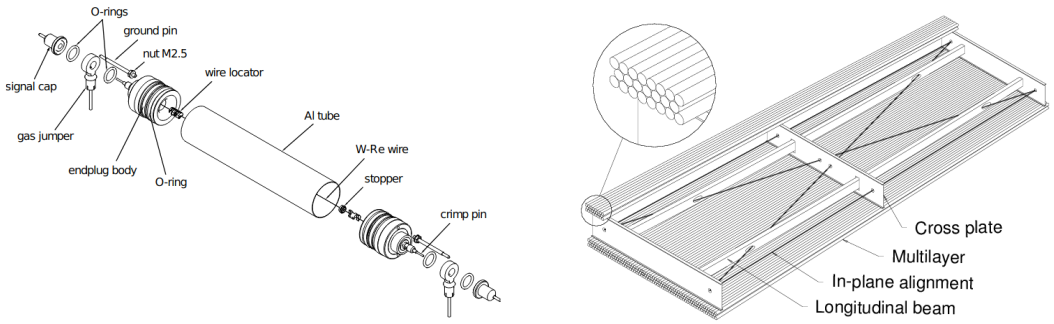

(a) Exploded view of a drift tube. (b) An MDT chamber.

Figure 1.9: Schematic view of MDT chambers.

Cathode Strip Chambers (CSC)

CSCs were located in the end-cap region $2 < |\eta| \leq 2.7$ in which the particle flux is quite high and thus exceeds MDTs safe operation limit. They belong to the family of multi-wire proportional chambers (MWPC) and they consist of wires, serving as anode and readout strips, hosted in two parallel layers, which serve as cathode. The distance between anode and cathode is equal to a wire pitch (1.10a).

They arranged in two disks with eight small and eight large chambers each containing four CSC planes (1.10b). The strips perpendicular to wires measure the principal coordinate (η), and the strips which are parallel to wires, provide the second coordinate (ϕ) measurments. CSCs were operating with a gas mixture of Ar:CO_2 and voltage of 1800 to 1900 V. They can achieve a resolution of 60 μm per CSC plane.

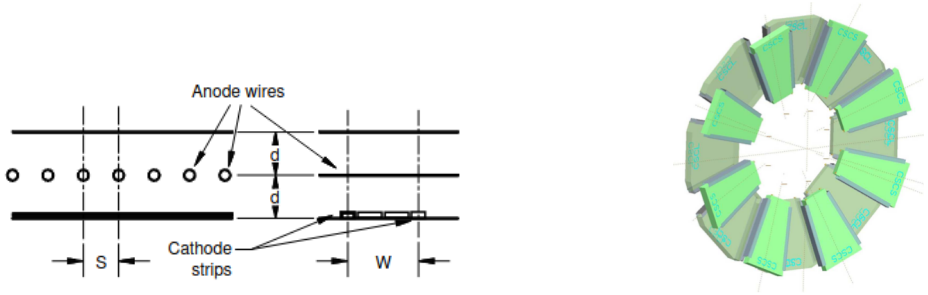

(a) CSC plane.

(b) CSCs layout.

Figure 1.10: Schematic view of CSC chambers.

Resistive Plate Chambers (RPC)

RPCs are part of the trigger system used in the barrel region ($\eta \leq 1.05$), and they are organised in three concentric cylindrical layers around the beam axis. They are gaseous parallel electrode-plate (no wire) detectors. The parallel electrodes are made of phenolic-melaminic (usually called bakelite) and they are kept parallel to each other at a distance of 2 mm by insulating spacers (1.11). The external surfaces of the plates are coated by thin layers of graphite painting in which a high voltage of 9.8 kV is applied. This generates a strong electric field which provides avalanche multiplication, through primary ionisations caused by the incident particles.

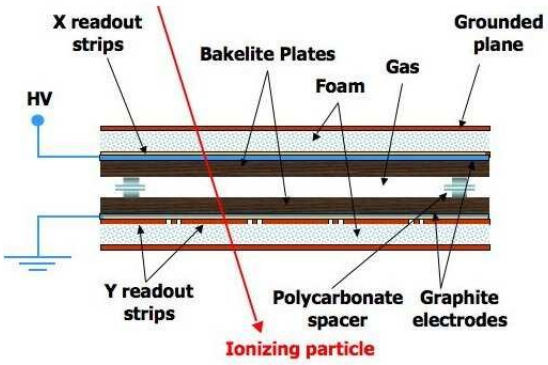

Figure 1.11: Structure of RPC chamber.

Between the parallel plates there is a gas mixture of $C_2H_2F_4$:C_4H_{10}:SF_6. The induced signal is read-out by strips that are placed orthogonal to each other in two independent layers, providing measurements on precision coordinate (η) and on second coordinate (ϕ). Their intrinsic time resolution of nearly 1 ns makes them a great candidate for the trigger system.

Thin Gap Chambers (TGC)

TGCs complete the trigger information in the end-cap region ($1.05 \leq \eta \leq 2.4$) but also determine the second, azimuthal coordinate (ϕ), to complement end-cap MDT's measurement in the bending (radial) direction.

TGCs, are also similar to Multi-Wire Proportional Chambers (MWPCs) with anode wires, enclosed by two graphite cathode layers and two layers of readout strips running perpendicularly to the wires (1.12). The radial, bending coordinate is measured by the wire groups while the azimuthal coordinate is measured by the radial strips. They operate with a highly quenching gas mixture of CO_2 and $n-C_5H_{12}$. The very intense electric field of 3200 V in conjunction with the small distance between the wires lead to very good time, momentum and azimuthal resolution requirements.

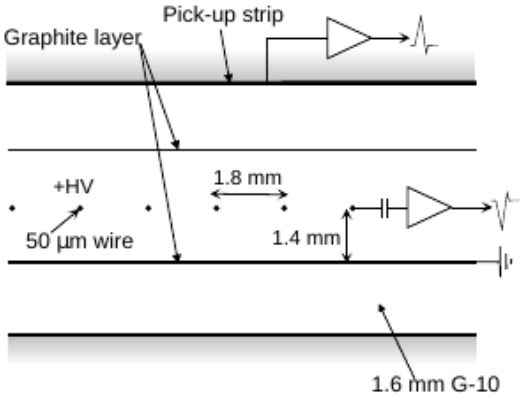

Figure 1.12: Structure of TGC chamber.

1.4.5 Trigger and Data Acquisition (TDAQ)

The trigger system is responsible for the selection of potentially interesting events, produced in each bunch crossing, and for their storage for later analysis. It can be divided in two distinct levels, (i) Level-1 (L1) and (ii) High-Level Trigger (HLT). Each trigger level refines the decisions made from the previous one, where necessary and applies additional selection criteria. Its goal is to reduce the rate of possible collisions from 40 MHz[4] to 1 kHz [12].

The L1 trigger consists of three subsystems, Level-1 calorimeter (L1Calo), Level-1 muon (L1Muon) and Level-1 topological trigger (L1Topo). It searches for high transverse-momentum muons, electrons, photons, jets and τ-leptons decaying into hadrons, as well as large missing and total transverse energy. Moreover in each event, L1 trigger defines one or more Region of Interest (ROI), that is, the coordinates, η and ϕ, of regions within the detector that the selection process has identified potentially interesting features. Lastly, L1 trigger reduces the initial particle collision rate from 40 MHz, to 100 kHz.

[4] since the proton-proton collisions take place every 25 ns

The HLT trigger is software-based and operates on a large farm of commercial computer processors. It executes chains of reconstruction and signature algorithms that analyse the properties of the events, reducing the rate of events up to 1 kHz.

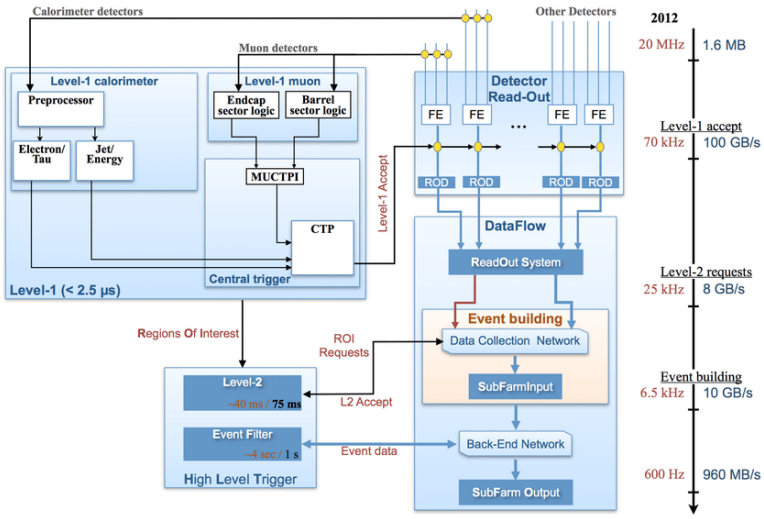

Figure 1.13: Schematic overview of the TDAQ system in Run 1.

The DAQ system is responsible for the transport and assembly of events' data from the front-end buffers to the permanent storage. If an event is accepted by the L1 trigger, the data are transferred to sub-detector Read-Out Drivers (RODs). Subsequently, the data pass to the Read-Out System (ROS), where they are buffered until requested by the HLT farm. In HLT they are assembled into events (event building) and ultimately recorded permanently.

1.4.6 Detector Control System (DCS)

From what it has been described until now, one could understand that an experiment such as ATLAS is a very complex system which must have the ability of being monitored and controlled remotely.

The DCS [13] permits the coherent and safe operation of the ATLAS detector hardware, and serves as a homogeneous interface to all sub-detectors and the technical infrastructure of the experiment. It allows to monitor, control and archive the operational parameters and signals. Furthermore, it permits automatic or manual correction actions, bringing the detectors into any desired operational state.

2 ATLAS UPGRADE

2.1 TOWARDS HIGH-LUMINOSITY LHC

The first operational run of LHC (Run 1) started on November of 2009, achieving 1.18 TeV energy per beam. Throughout the first run, LHC reached an energy of 3.5 TeV per beam and distributed an integrated luminosity[1] of nearly 29 fb^{-1}, resulting in a vast quantity of physics results. One of the highlights was the observation of the Higgs Boson. The very successful first LHC run came to an end in December 2012, followed by a major shutdown of LHC, the so called Long Shutdown 1 (LS1). During this two-year period, LHC as well as, Proton Synchrotron (PS) and Super Proton Synchrotron (SPS), underwent a series of upgrades and maintenance activities.

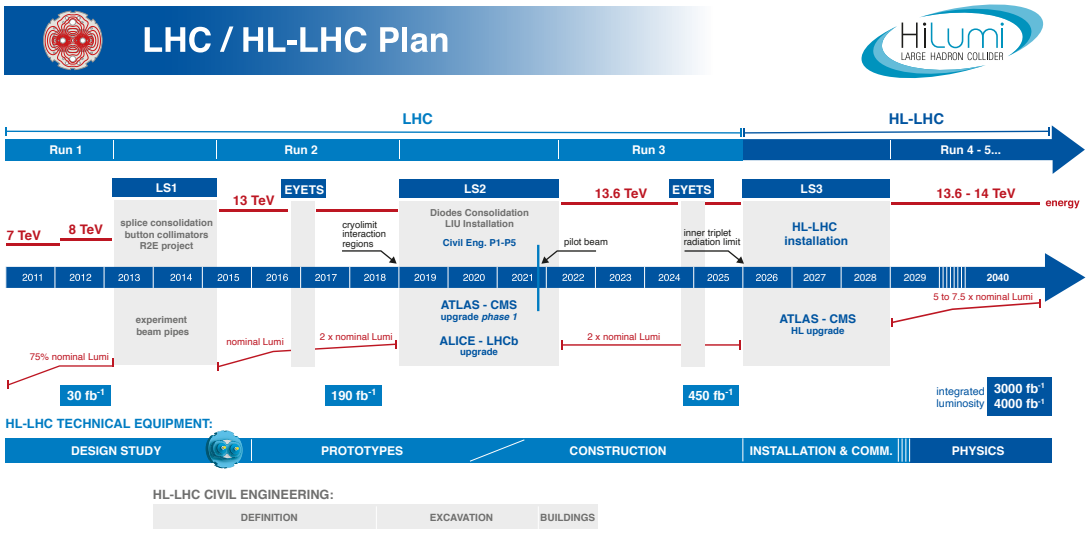

Figure 2.1: High Luminosity LHC schedule.

In 2015, the second operational run (Run 2) was launched achieving an energy of 6.5 TeV per beam and reducing the Bunch Crossing (BC) timing at 25 ns. On December of 2018, Run 2 was ended. LHC, in order to further increase its discovery potential, had to undergo two long shutdown periods

[1] Integrated luminosity measures the total number of collisions produced over a period of time.

(2.1) aiming to increase instantaneous luminosity (rate of collisions) by a factor of 5 to 7.5 beyond the original design value and integrated luminosity by a factor of 10 [14]. This increase is believed to result in more statistics that would provide more accurate measurements on existing and possibly new phenomena while enabling the observation of rare processes.

Experiments, in order to cope with the new conditions that would be imposed by High-Luminosity LHC (HL-LHC) have also to upgrade their systems. The upgrades designed to be performed in two phases (I & II), two different periods of time. The Phase I (LS2) took place during the past years (December 2018 - April 2022), mainly focusing on the Level-1 trigger for both muon and calorimeter systems. The major updates during this period were, (i) the NSW (ii) integrating it into L1 logic (iii) implementing a new readout system and (iv) upgrading LAr calorimeters electronics.

The finalisation of upgrades for the HL-LHC will take place in the Long Shutdown 3 (Phase II). Several updates are foreseen to be applied on calorimeters, the muon system, the inner tracker, on TDAQ and on computing and software.

2.2 Motivation of Small Wheels replacement

Studies have shown that in the era of HL-LHC, the performance of the muon tracking chambers (in particular in the end-cap region) degrades with the expected increase of cavern background rate. More specifically, an extrapolation from the observed rates at the lower luminosity conditions of the 2012 run, to high luminosity and high energy conditions, indicated a substantial degradation of tracking performance, both in terms of efficiency and resolution in the inner end-cap station, as can be seen in 2.2 plot.

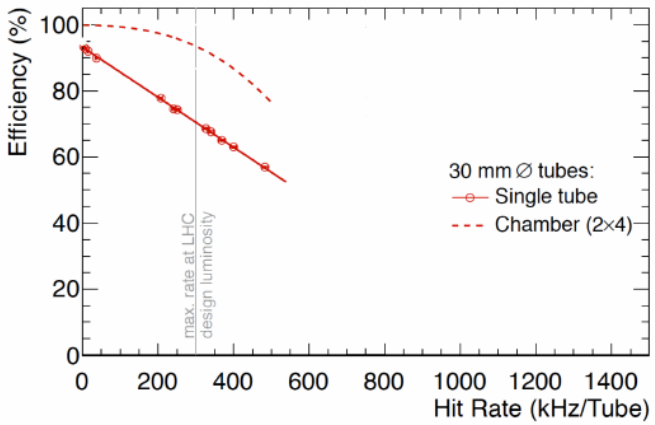

Figure 2.2: Efficiency of MDT tube hit (solid line) and track segment efficiency (dashed line, referring to a MDT chamber with 2x4 tube layers) as a function of tube rate estimated with test-beam data. Design luminosity corresponds to 1×10^{-34} cm^{-2} s^{-1} [15].

Furthermore, analysis of 2012 data demonstrated that a significant part of the muon trigger rate in the end-caps is due to background. Low energy particles, mainly protons, generated in the material

located between the Small Wheel and the EM station, produced fake triggers by hitting the end-cap trigger chambers at an angle similar to that of real high p_T muons. The following plot (2.3) depicts that nearly the 90% of muon triggers were fake.

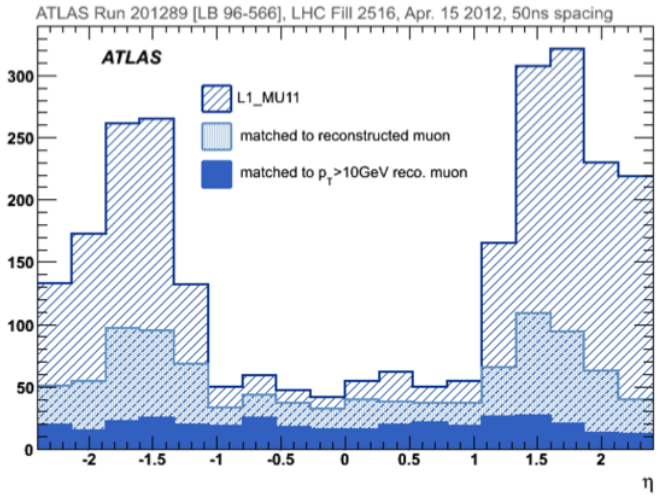

Figure 2.3: Pseudorapidity distribution of muon ($p_T > 10$GeV) signal (L1_MU11 in plot) superimposed with offline well reconstructed muon candidates, combining inner detector and muon spectrometer track with $p_T > 3$GeV and offline reconstructed muons with $p_T > 10$GeV [15].

In order to solve all of those problems, ATLAS proposed the replacement of muon Small Wheels with the "New Small Wheels". The NSW consists of a set of precision tracking and trigger detectors able to operate in a high background radiation region, up to 15 kHz/cm^2, while reconstructing muon tracks with high precision as well as furnishing information for the Level-1 trigger.

2.3 New Small Wheel (NSW)

The NSWs [15] were designed to address all requirements presented in the previous chapter in order to preserve the good performance of ATLAS experiment. The detector technologies which were chosen are the MM and the sTGC. The MM are primarily deployed for precision tracking, given their high spatial resolution, while the sTGC are deployed for triggering given their single bunch crossing identification capability. However, the two detector technologies also complement each other for their corresponding primary functions.

As their name suggest, NSW are wheel shaped, consisting of sixteen (16) sectors, eight (8) big and eight (8) small (fig. 2.4). Each sector is divided into four multilayers, sTGC – MM – MM – sTGC

(fig. 2.5b). The arrangement has been chosen in such way so as to maximise the distance between the sTGC multilayers, since this detector configuration is optimal for the online track resolution[2].

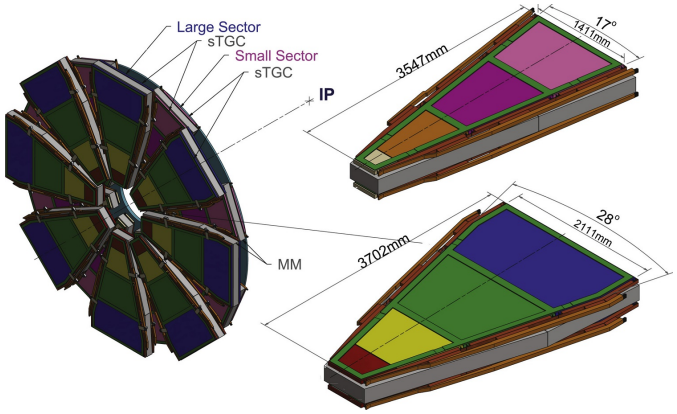

Figure 2.4: **Left:** NSW schematic representation. **Right:** Sectors' view (small up and large down).

Each multilayer comprises of four sTGC and four MM detector planes, which is called wedge. The choice of eight planes per sector was dictated by three reasons. The first one was the need of a robust and fully functional detector system over its whole lifetime, since NSW is expected to operate for the whole life of the ATLAS experiment. The second reason was the need to ensure an appropriate detector performance, even if some planes fail to work properly. Finally, the third reason stems from the high background that this region faces. With eight planes per detector, tracks will be reconstructed reliably and with high precision under these conditions.

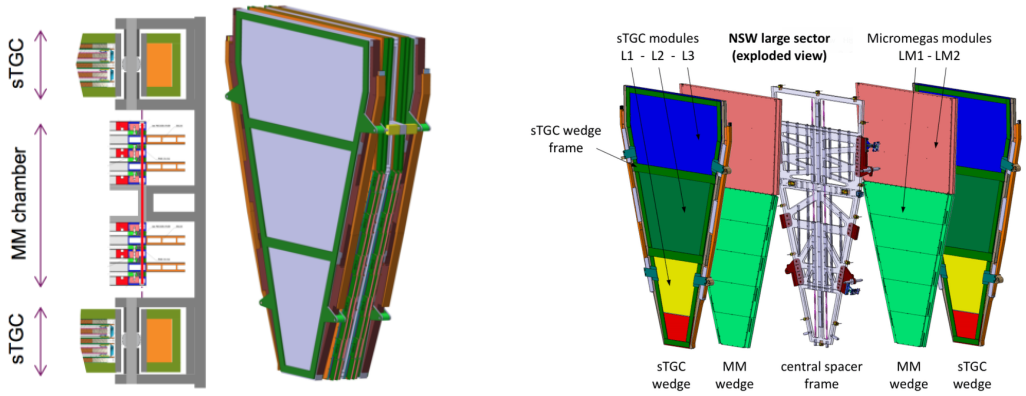

(a) Sector's profil.

(b) Exploded view

Figure 2.5: Schematic representation of sectors.

[2] As online track hits are reconstructed with limited accuracy, increased distance between detector multilayers leads to an improved online track segment angle reconstruction resolution.

3 Detector technologies of NSW

3.1 small-strip Thin Gap Chambers

As it has already been mentioned, HL-LHC would impose a high background environment. As a result, a modification of TGC detector technology was mandatory in order to achieve a very good (nearly 100 μm) position resolution at high count rates. From the aforementioned necessity sTGC were born, which as an improved version of TGC, are also a variant of the MWPC introduced by G. Charpak and his collaborators in the late 1960's [16].

Their basic structure is shown in figure 3.1. They consist of a grid of 50 μm gold-plated tungsten wires with a 1.8 mm pitch, sandwiched between two cathode planes at a distance of 1.4 mm from the wire plane. The cathode planes are made of a graphite-epoxy mixture with a typical surface resistivity of 100 kΩ/□ sprayed on a 100 μm thick G-10 plane. Behind the cathode planes, there are strips one side (that run perpendicular to the wires) and on the other side pads (covering large rectangular surfaces). These pads are mounted on a 1.6 mm thick PCB with the shielding ground on the opposite side. The chambers are filled with a gas mixture of CO_2:n−pentane (55:45).

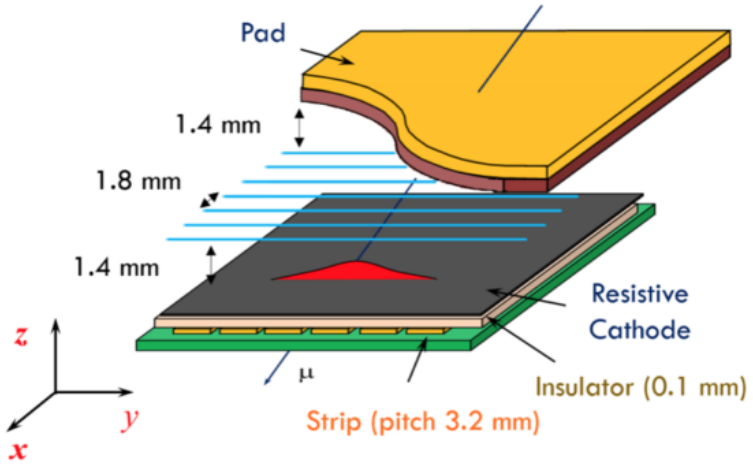

Figure 3.1: Internal structure of sTGC.

The charge of all strips, pads and wires are readout for offline track reconstruction. The pads are utilised to produce a 3-out-of-4 coincidence, in order to identify muon tracks roughly pointing to the interaction point. They are also used for defining which strips should be readout to obtain a precise

measurement in the bending coordinate, for the online muon candidate selection. The azimuthal coordinate, for which only about 10 mm precision is needed, is obtained from grouping wires together.

3.2 Micromegas

MM is an abbreviation of Micro-MEsh Gaseous Structure, a gaseous detector coming from the development of the wire chambers. It was developed by Y. Giomataris and his collaborators in the middle of 1990's [17]. A typical structure of a MM detector is depicted in the following figure. It comprises of a planar (drift) electrode, a gas gap of a few millimeters thickness acting as conversion and drift region, and a thin metallic mesh at typically 100 to 150 μm distance from the readout electrode, creating the amplification region. The drift electrode as well as the amplification mesh are at negative high voltage potentials, while the readout electrode is at ground potential.

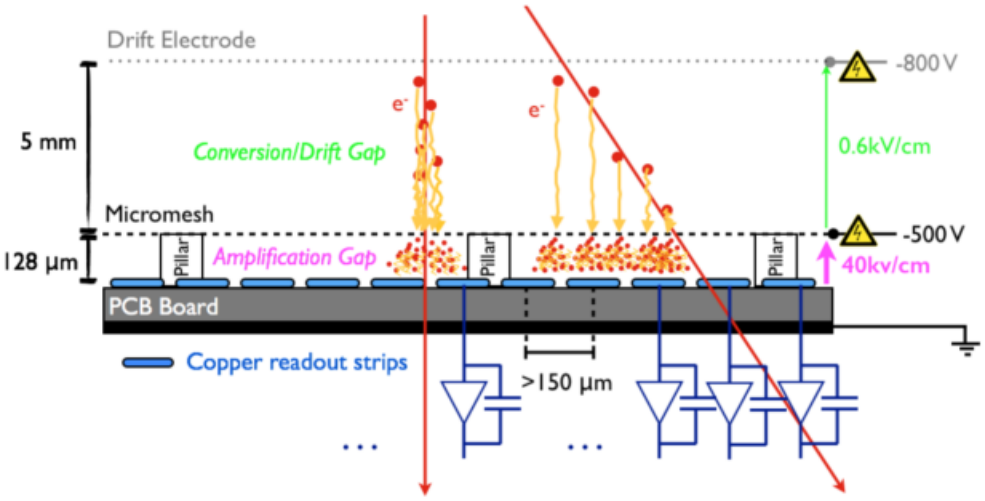

Figure 3.2: Layout and operating principle of MM detector.

As charged particles cross the detector, they ionise the gas, releasing electrons which drift towards the mesh, while positive ions drift towards the drift electrode. Electrons, approaching the mesh "encounter" a 50 to 100 times stronger electric field making mesh transparent to more than 95% of electrons. Accelerated by the much higher electric field of amplification region, they collide with far more gas molecules, and thus freeing much more electrons, producing the so called Townsend avalanche[1] (or Townsend discharge).

3.2.1 Resistive strip Micromegas (MM)

Although, MM have exceptional characteristics, making them the most suitable choice for the upgrade, the very thin amplification region along with the finely sculpted readout structure, makes them

[1] Name after the John Sealy Townsend, who discovered the fundamental ionisation mechanism.

particularly vulnerable to discharges (sparks). Sparks occur when the total number of electrons in the avalanche reaches nearly 10^7 and are quite dangerous since they may damage the detector and readout electronics and/or lead to large dead times as a result of HV breakdown.

In order to detect with high detection efficiency minimum ionising muons, amplification factors of the order 10^4 are needed. Therefore, ionisation processes[2] that produce more than a thousand electrons at comparable distances to the lateral extension of an avalanche (some hundreds of μm) can produce dangerous discharges. Since the NSW lies in the end-cap region in which particle rates can reach the order of 15 kHz/cm^2, the risk of sparks is quite high for the MM.

For those reasons, the MAMMA (Muon Atlas MicroMegas Activity) Collaboration developed an anti-spark protection [18] by adding a thin layer of insulator (64 μm thick) on top of which strips of resistive paste (with a resistivity of a few MΩ/cm) are deposited parallel to the readout strips (fig. 3.3). The purpose of the spark protection layer is to limit, in the event of a spark, the discharge currents to a level so that drops of the high voltage of the mesh become insignificant.

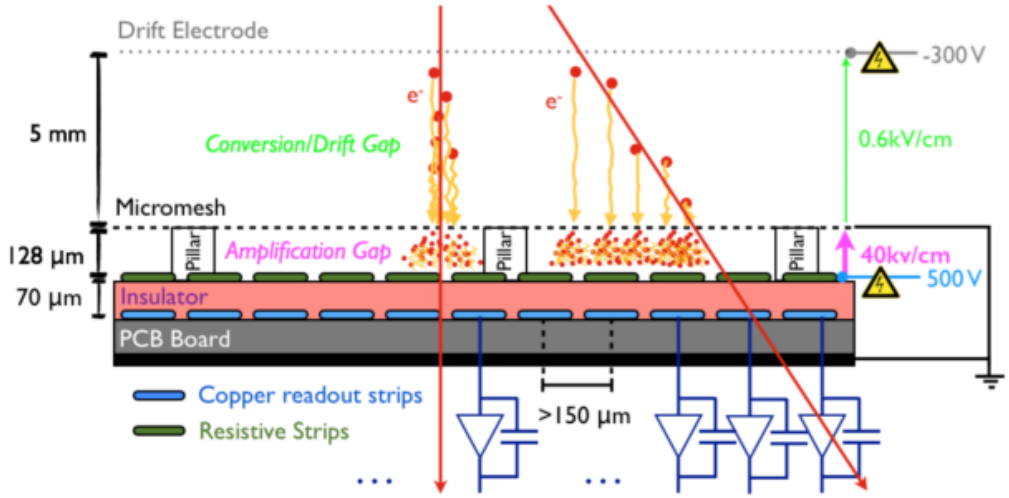

Figure 3.3: Layout of resistive MM detector.

3.3 NSW's electronic system overview

Apart from the new detector technologies, a new system of electronics for the readout and trigger processing had to be designed in order to cope with the new requirements imposed by HL-LHC [19]. The acquisition of primitive data is done through three new Front-End (FE) boards, due to the different characteristics of the two detector technologies. The Micromegas Front-End 8 (MMFE8), the strip Front-End Board (sFEB) and the pad Front-End Board (pFEB). The first one as can be deducted from its name is used from MM detector while the other two from sTGC. Moreover, intermediate boards

[2] Such ionisation levels are easily reached by low-energy alpha-particles or slowly-moving charged debris from neutron (or other) interactions in the detector gas or detector materials.

had to be designed such as, the L1DDC and ADDC, in order to further propagate the data to the next steps of process logic. The boards house a number of new ASICs, specifically designed to operate under the harsh environment created by the radiation and the strong magnetic field.

3.3.1 MicroMegas Front-End 8

This board [20] is located on MM detector and its purpose is to gather the primitive data from detector's strips. This is done through the eight VMM [21] that it hosts. Each channel, has discriminators and Analog to Digital Converters (ADCs) sending data to both trigger and readout path. VMM has 64 channels in total, each channel connected to a strip of the detector, meaning that a single MicroMegas Front-End 8 (MMFE8) is able to read-out 512 strips of MM.

A MMFE8 also hosts the GBT-SCA ASIC [22], part of the GBT chip-set. Its purpose is to distribute control and monitoring signals to the on-detector front-end electronics and perform monitoring operations of detector environmental parameters. Furthermore, MMFE8 houses the ROC [23], responsible for the transition of data streams from the eight VMMs to the L1DDC and more specifically to the Giga-Bit Transiver (GBT) based on the ATLAS Level-0 trigger (readout path).

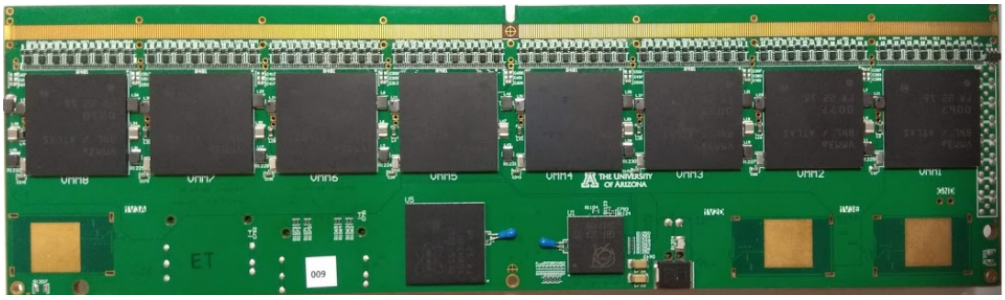

Figure 3.4: The underside of a production MMFE8. In the upper part there are the 8 VMMs. On down left there is the ROC and next to it the SCA ASIC.

3.3.2 Level-1 Data Driver Card

The L1DDC [24] serves as an intermediate board that establishes a bidirectional connection between front-end electronics, and Front-End LInk eXchange (FELIX) [25]. It has been designed for the needs of NSW upgrade by NTUA's experimental high-energy physics team, but it can be used in any readout system, since it is completely transparent to the data transmitted or received. Due to the different characteristics of NSW's detectors, there have been created three different types of L1DDC, one for MM detector and two for sTGCs.

Its function is achieved through the GBT project's architecture [26], in which CERN's microelectronics group, has developed electronic components capable of sustaining high radiation doses. The GBT project comprises of, GBTx ASIC, the GigaBit Transimpedance Amplifier (GBTIA), the Gigabit Laser Driver (GBLD) as well as GBT-SCA.

GBTx is a serialiser - deserialiser chip receiving and transmitting serial data at 4.8 Gb/s. In our case, GBTx receives the data from Front-End boards and more specifically from ROC, upon L1 signal, transmits them to FELIX and also transmits reference clock, slow control and trigger data from FELIX to Front-End boards.

GBTIA is a trans-impedance amplifier receiving the 4.8 Gb/s serial input data from a photodiode and GBLD is a laser-driver ASIC which modulates 4.8 Gb/s serial data on a laser. The aforementioned ASICs are used by the Versatile Transceiver (VTRx) [27], a bidirectional opto-electronic module that is used for the optical data transmission from on-detector electronics to off-detector electronics and vice versa.

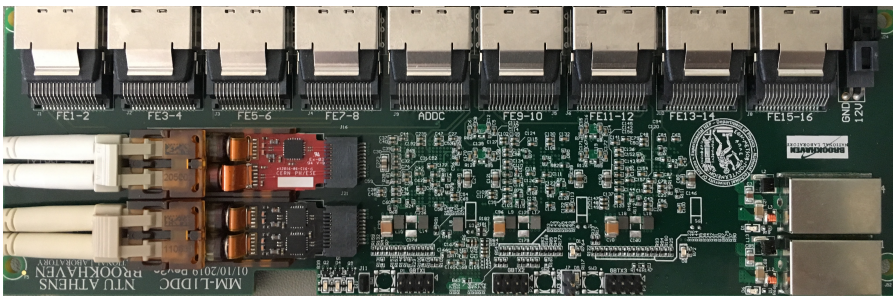

(a) A photograph of the upper part of L1DDC. On *top* there are nine miniSAS connectors (eight for MMFE8s and one for the ADDC). On *bottom* left we have the VTRx and VTTx while on *bottom* right we have the two FEAST ASICs.

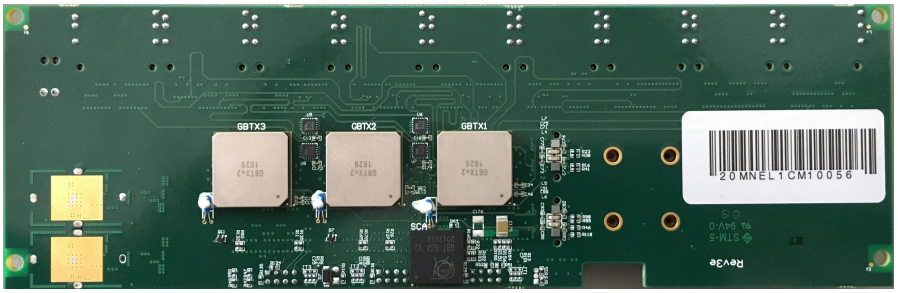

(b) A photograph of the bottom part of L1DDC. On *top* there are the three GBTXs and below them the SCA ASIC.

Figure 3.5: The L1DDC board for MM detector.

3.3.3 ART Data Driver Card

The ADDC board [28] has been designed for the MM detector, to process and transmit the trigger data from the Front-End ASICs to the trigger processor. More specifically in every bunch crossing, the 64-channel VMM ASIC provides an encoded 6-bit address of the first above-threshold hit channel. This 6-bit address composes the ART (Address in Real Time) signal.

The hit selection is processed by a custom ASIC named ART. ADDC board houses two ART ASICs each of which can handle up to 32 ART signals[3]. Two GBTx ASICs collect the selected data from the two ART ASICs and transmit them through the unidirectional Versatile Twin Transmitter (VTTx).

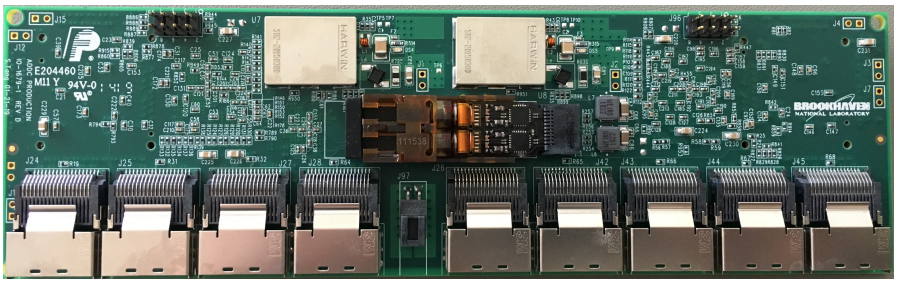

(a) A photograph of the upper part of ADDC. In the *bottom* there are nine miniSAS connectors (eight for MMFE8s and one for the ADDC) and above them the VTTX.

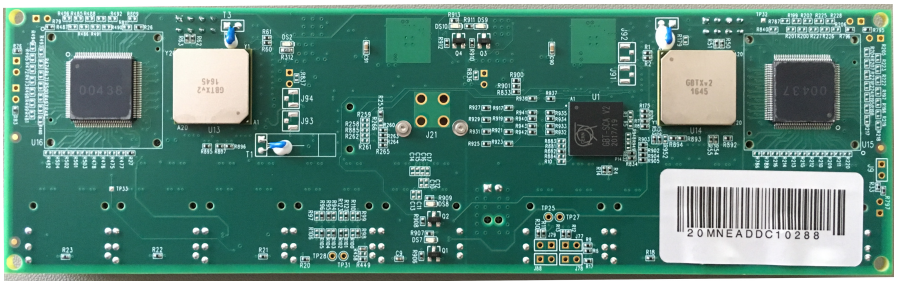

(b) A photograph of the bottom part of ADDC. In the outer part there are the two ART ASICs. Moving towards the center, there are the two GBTXs and the SCA ASIC.

Figure 3.6: The ADDC board.

[3] That is, each ART ASICs can collect data from 32 VMMs or 4 MMFE8s

Part II

ATLAS DETECTOR CONTROL SYSTEM

4 Detector Control System

4.1 Introduction

It goes without saying that large experiments, such as the ones that CERN hosts, due to their enormous size, complexity and the hostile environment under which they operate, need a "way" to be monitored and controlled remotely. Given these reasons, a system that allows the control and supervision of detectors' operations over the lifetime of the experiments, is mandatory.

The system that is used to ensure the consistent and safe operation of ATLAS's sub-detectors, as well as the common experimental infrastructure along with their supervision is called Detector Control System (DCS) [29]. DCS, allows the transition between the possible operational states of the detector, while in parallel, it performs constant monitoring and archiving of the system's operational parameters. In case of any irregular behaviour it issues an alarm requiring immediate actions. These actions can be either manual of automatic depending on the type of alarm.

4.2 Design of system

DCS was designed and implemented within the frame of the JCOP [30], a collaboration of CERN control group and DCS teams of the LHC experiments. JCOP combines common standards for the use of DCS hardware, based on a Supervisory Control and Data Acquisition (SCADA) system, WinCC Open Architecture (formerly known as PVSS[1]) by Siemens which serves as the basis for all DCS applications.

The architecture of ATLAS DCS can be divided in two categories, the Front-End (FE) equipment and the Back-End (BE) system. The Front-End (FE) equipment, comprises of custom made electronics and their related services such as, high voltage power supplies, cooling circuits etc. The Back-End (BE) system uses WinCC OA which utilises the interface between the Front-End control systems and the components of JCOP framework, to facilitate the integration of standard hardware devices and the implementation of homogeneous control applications. The Back-End is organized in three layers (fig. 4.1), (i) The Local Control Stations (LCS) that are directly connected to Front-End equipment and performs the low-level monitoring and control of different systems of detector services. (ii) The Sub-detector Control Stations (SCS), which are responsible for full control of the sub-detectors and (iii) the Global Control Stations (GCS) that perform the overall control of the detector equipment, through service applications and operator interfaces. [31].

[1] The old name of WinCC OA before the acquisition of ETM by Siemens.

The interface between Front-End (FE) and Back-End (BE) used to be through OPC industry standard, but due to its platform restrictions and its expiring long-term support, it has been replaced by OPC Unified Architecture (UA) [32] standard.

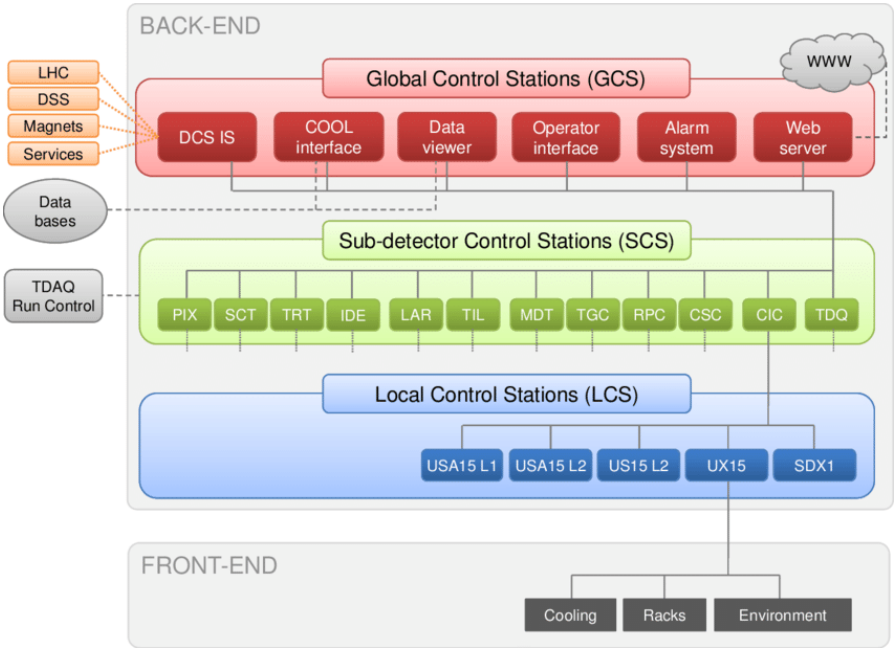

Figure 4.1: ATLAS DCS architecture.

The complete hierarchy of Back-End (BE) system is represented through a FSM, integrating more than 10 million data elements into a single tree structure, ensuring proper operation and efficient handling of errors.

4.3 WinCC Open Architecture

WinCC OA is an object-oriented software package designed for the use in automation technology. It provides a comprehensive set of tools and features for monitoring, controlling, and visualizing industrial processes in real-time. Its operation relies on gathering information from the FE equipment and offers supervisory control functions such as data processing, execution of control procedures, alert handling, trending, archiving and web interface. It has been selected among other SCADA candidates due to its openness, scalability and platform independence.

4.3.1 Architecture overview

WinCC OA's architecture [33] is divided into layers (fig. 4.2). Each layer consists of specific units, that utilise the required functionalities depending on the task that they are assigned. These units are

called *managers* and they communicate through a specific protocol of WinCC OA, TCP/IP. Its architecture can be distributed within *multiple* computers forming a system (even with different managers running on each one) that can also run on different operating systems. Its internal architecture is also entirely event-driven, allowing a significant reduction of the data traffic leading to better performance, compared to other SCADA based products. The included managers are described in detail below.

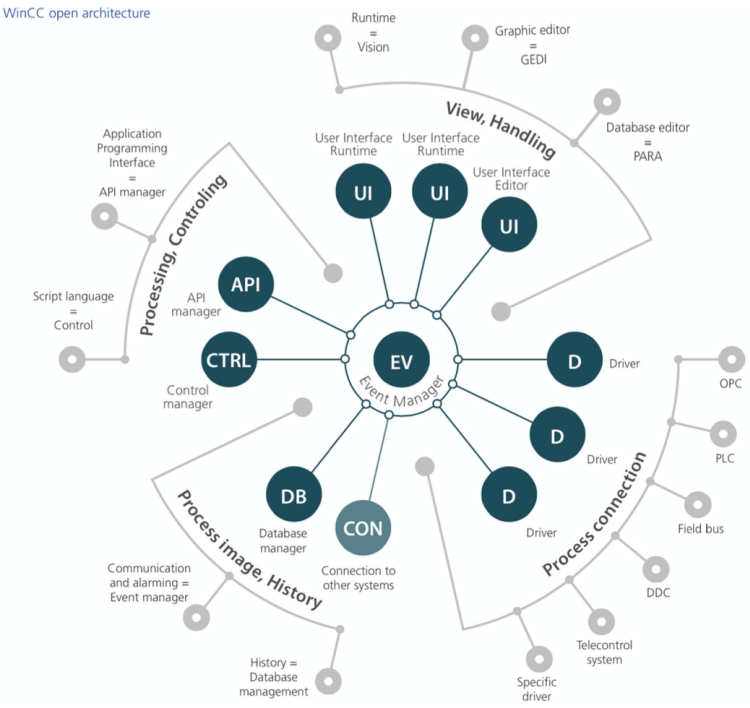

Figure 4.2: Architecture of a typical WinCC-OA system and the set of managers it consists of.

Process interface layer

The process interface modules, which are also called drivers (D), form the lowest level of a WinCC OA system. In simple terms, drivers are programs that convert certain protocols of the externally connected devices into the internal communication form of WinCC OA. Since there are numerous different communication forms with PLCs or other remote control nodes, there are several different drivers available, such as, OPC, ModBus, Ethernet IP, etc. Drivers are able to read current states, measured values or counter values from the field and they pass commands and set values to the subordinate devices.

Process image and history layer

Event manager (EVM), is the *heart* of the system, being the central processing center of WinCC OA, responsible for all communications. This unit always keeps a current image of all process variables in memory. Any other manager that needs access to data, receives the data from the process image

(the current value of all data) of the event manager and does not have to communicate directly with a control unit. Moreover, event manager executes the alert handling and is able to execute different stand-alone calculating functions.

In the same layer we also have the data manager (DB) that supports event manager, providing a link to a database where values and alerts are stored. Furthermore, it handles the configuration of the data that are stored in the database. The database is accessed via SQL language, where the query is executed by the data manager and *not* the database itself.

Processing and control layer

WinCC OA gives numerous possibilities to implement algorithms and processings. The most important are internal control language (CTRL) and the common application programming interface (API).

Control, is an advanced procedural high level language based on the syntax of ANSI-C that provides a wide function library for control tasks and visualisation technics. Control can be used as standalone process (Control manager), for animation and user interface design (UI manager) or for standardise data-object based processing (Event manager).

API is a C++ class library that allows the software developer to implement individual functions as an independent additional manager (prognosis system, simulation, etc). Moreover, it allows access to the run-time database of the product, facilitating in our case the interface between the DCS and the external systems like the LHC accelerator, or the DAQ system.

Visualization and operation layer

The visualization of graphics is handled by the User Interface manager (UI) whose most important parts are, the Graphics EDItor (GEDI), the database editor (PARA) and the general user interface of the application (VISION).

GEDI (fig. 4.3a) gives users the ability to create their own graphical user interfaces (panels) using a set of objects such as, buttons, tables, text fields etc. Each object has a list of events which can be programmed according to users' needs and give the desired results when triggered.

WinCC OA defines structured, device orientated data points (DP) in order to manage, integrate and visualise system's data. The data points are defined in a tree structure with arbitrary branching levels. The parent "node" of this tree is called data point type (DPT)[2] and it corresponds to a mechanical system or an integrated set of their sub-units, for example, a type of high voltage board or a temperature sensor. Data points are the next "node" in hierarchy and they refer to a more specific device of the system or to a set of properties. For example, it would be a specific high voltage board that serves a part of the detector. The next "node" in hierarchy are the data point elements (DPE) that correspond to a value or state of data points. An example would be the value of operational voltage, or the standby

[2] In the object-oriented software engineering you would call the data point type a "class" and the representation of an individual device (the data point) an instance.

voltage of the chamber. PARA is a graphical interface used to view, create and edit data point types and data points (fig. 4.3b).

VISION is the graphical interface that allows fast test of user interfaces (panels) under development.

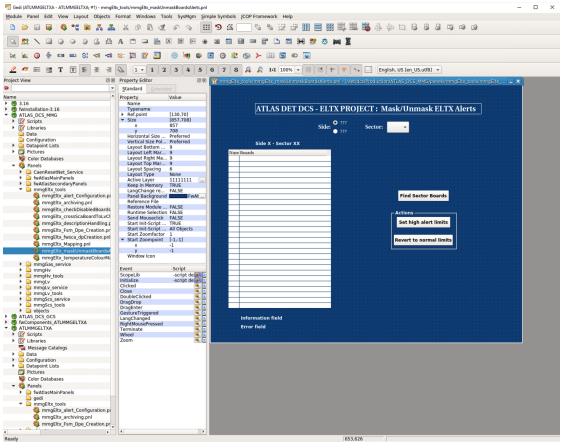

(a) An instance of Graphics EDItor (GEDI).

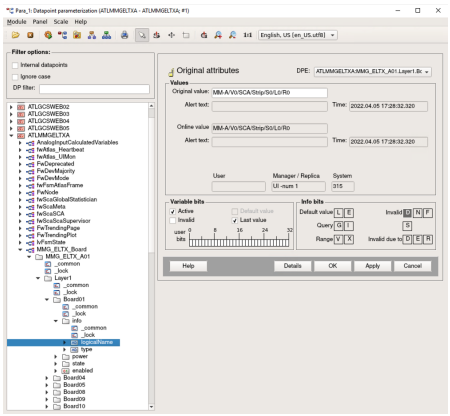

(b) An instance of database editor (PARA).

Figure 4.3: Pictures of WinCC OA user interface.

4.4 Joint COntrols Project (JCOP)

The JCOP framework was designed to provide common control solutions for the four experiments by JCOP team, a collaboration between CERN and LHC experiments. The motivation behind this collaboration was to identify common needs and provide common tools and solutions that the four experiments can use as a basis, for the development of their final control systems.

In simple terms, JCOP framework is an integrated and coherent set of guidelines, devices and tools that are required by all four experiments. It serves as a layer on top of WinCC OA and the other tools in order to simplify their use for the application developers. The framework has been splitted into a series of components for better management, since the requirements of an experiment or a detector technology are not necessarily needed by others. Some of the most notable tools/components are, the Access Control component, the OPC UA tools, the RDB archiver, the trending tool, the XML parser, the FSM toolkit etc.

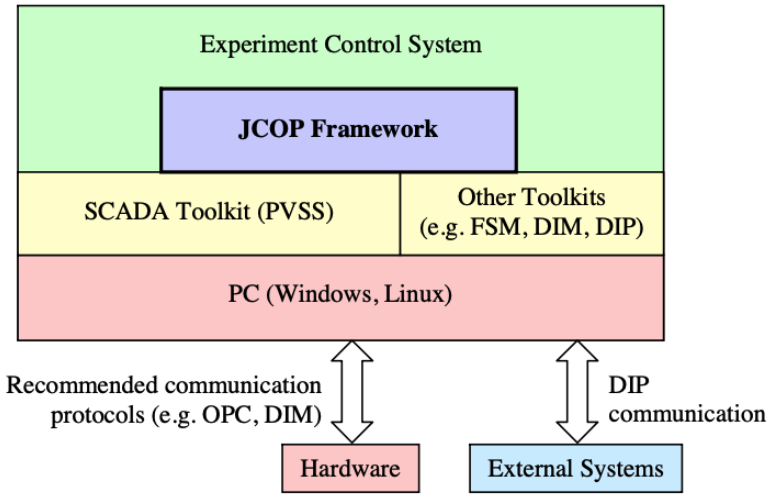

Figure 4.4: The JCOP framework.

4.5 Finite State Machine (FSM)

As we have already mentioned in section 4.2, the back-end system of ATLAS DCS is modelled by a Finite State Machine (FSM). An FSM is a mathematical model of computation, an abstract machine that can be in exactly one of a finite number of states at any given time and to change from one state to another, in response to some inputs. It constitutes a simple and efficient way to describe large-scale control systems by breaking down into small and simple objects that can be controlled and monitored not only individually, but also in an hierarchically unified way.

The JCOP framework provides a generic, platform-independent and object-oriented implementation of state machine toolkit, interfaced to WinCC OA software, giving the ability to develop FSMs based on each sub-detector needs and uniqueness.

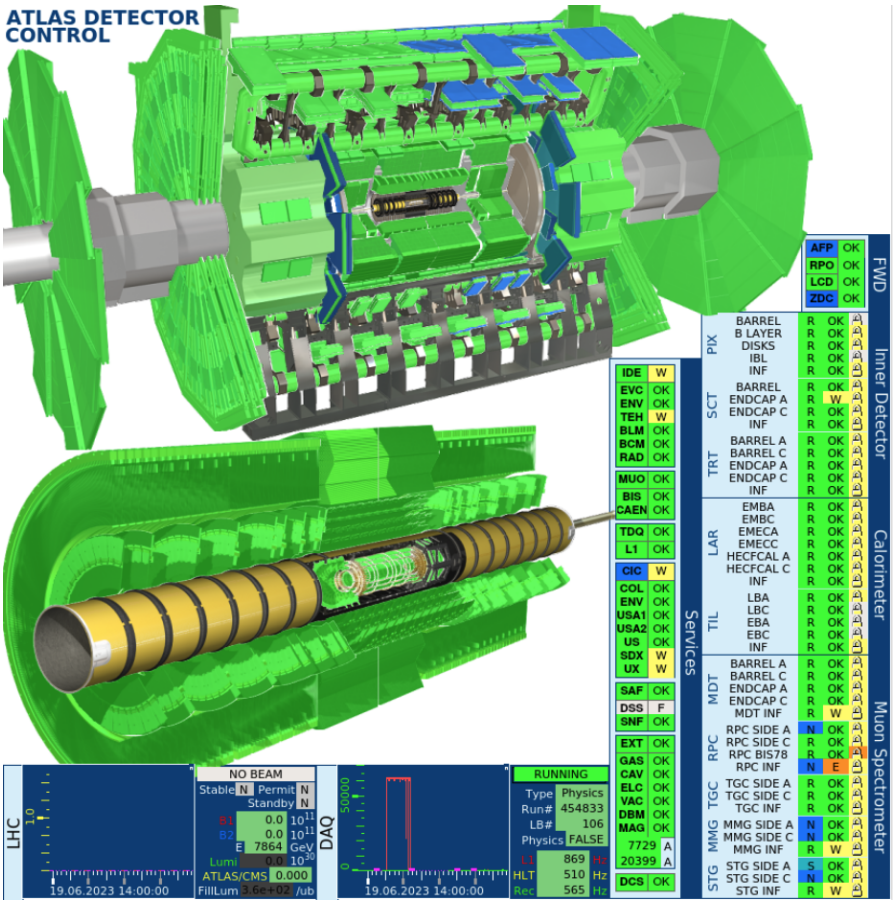

Figure 4.5: The general user interface of ATLAS FSM.

Each sub-detector, follows a parent-child hierarchical logic structure, and combined all together form the general ATLAS FSM (fig. 4.5). The architecture of tree's hierarchy is based on the functionality and the position of each part of the tree (also called node). There are three different type of nodes that can be defined, (i) the Device Units (DU), that represent the hardware reflecting their actual state and status. (ii) The Logical Units (CU), that hold a higher hierarchy level, containing several DUs, monitoring their state and status without the ability of passing commands to them and (iii) the Control Units (CU), that are slightly more complex objects, containing several LUs and/or DUs monitoring their state and status with the ability of passing commands to them.

The *state* defines the operational mode of a system or a part of a system. Some examples would be, "READY", "TRANSITION" or "SHUTDOWN". *Status* gives more details about how well the system works. Examples of status are, "OK", "WARNING" etc. The state and status are propagated

from lower levels nodes to the top, while the commands are passed from top level nodes to the lower ones.

4.6 Alarm screen

Along with the FSM, the alarm screen (fig. 4.6) is the second user interface that is used for the monitoring and the operation of DCS. Its mission is to display, in real time, the list of active alarms that have been occurred from hardware or software malfunction, categorised according to their severity in, "WARNING", "ERROR" or "FATAL". The occurrence of an alarm also appears in the corresponding FSM node.

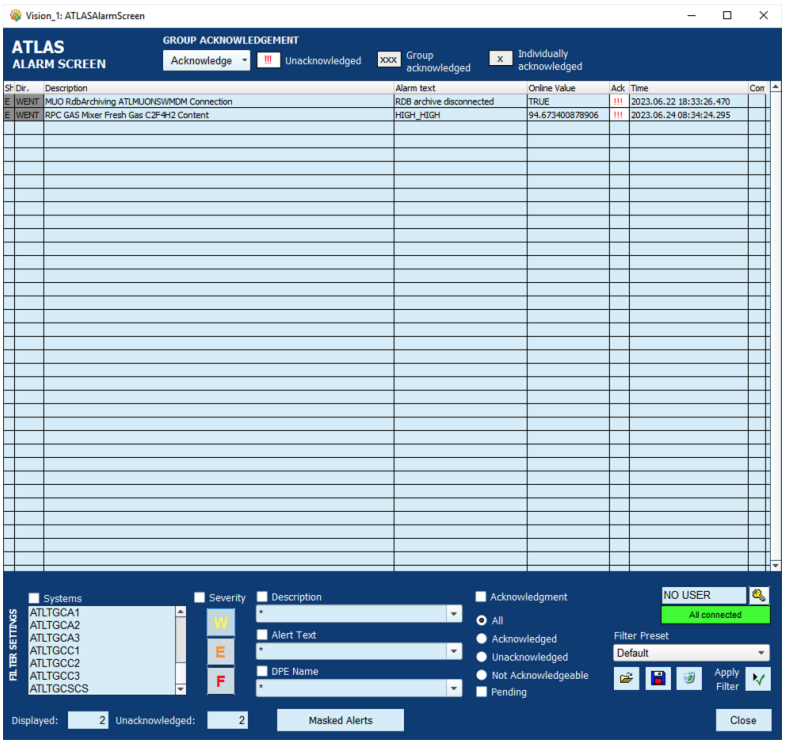

Figure 4.6: An instance of muon alarm screen.

Alarm screen permits the rapid detection of possible problems that may occur to the detector, allowing users (shifters and experts) for identification of the problem and better follow up. The user interface gives the ability to filter alarms based on the system, the different alarm attributes and provides the possibility of quering the alarm history, contributing in the safe and efficient operation of ATLAS detector.

5 Development on New Small Wheel Detector Control System

5.1 New Small Wheels' FSM architecture

Since NSW comprises of two detector technologies, two new nodes have been added under the muon FSM, in order to monitor and operate each of the two detectors independently. The internal architecture of each detector's FSM is divided into two, imaginary levels. The first one is based on their geographical position, side A & C and their infrastructure. The second one is based on their services, High Voltage (HV), Low Voltage (LV), Electronics (ELTX) and the MDT Device Module (MDM) [34] (fig. 5.1). All of the services follow the detectors' geographical position, meaning they are divided in sectors, multiplets, layers etc.

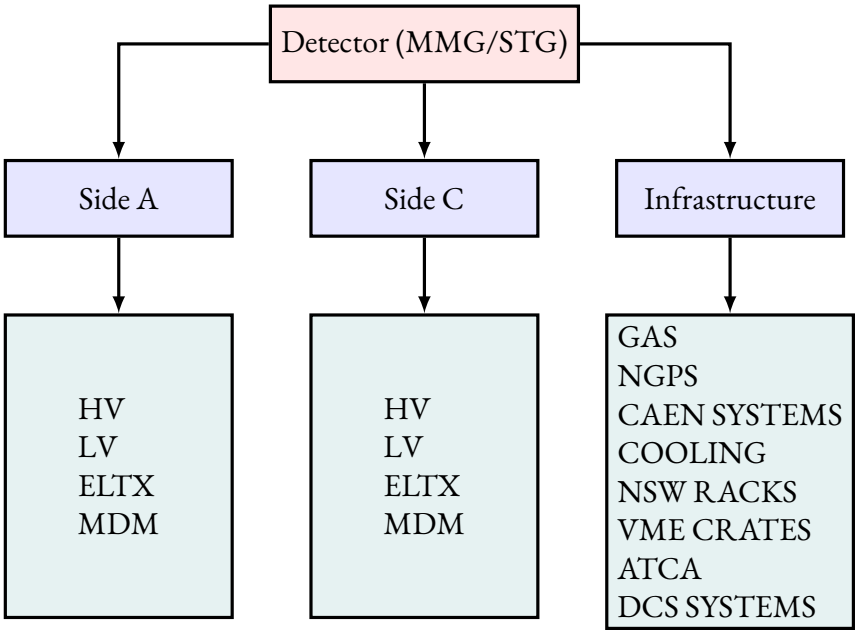

Figure 5.1: Schematic overview of MM and sTGC FSM tree map.

The following sections will focus on electronics (ELTX) and the contributions that have been made in the context of this thesis.

5.2 Electronic's (ELTX) FSM architecture

The electronic boards that have been installed on detectors (mentioned in section 3.3) are monitored and controlled through the dedicated part of each detector's FSM. Choosing a sector (fig. 5.2a) and a layer (fig. 5.2b), one can navigate to the desired board and monitor the various parameters such as, temperature of its components, voltage, connectivity to OPC UA server etc.

(a) Sector's view.

(b) Layer's view.

Figure 5.2: Electronic's FSM.

5.3 NSW XML generator

Generally speaking, distributed control systems require middleware software, which transfer data between components of a distributed system. The middleware software that has been chosen by ATLAS DCS is the OPC Unified Architecture (UA). In order to help developers unfamiliar with the OPC UA standard and to reduce development and maintenance costs, the team of ATLAS central DCS has developed a framework that creates (generic) OPC UA servers [35]. The only prerequisite for the framework is a design file, in XML[1] format, describing an object-oriented information model of the target system or device. Using this model, the framework generates an executable OPC UA server application, which exposes the per-design OPC UA address space, without the developer writing a single line of code.

In the case of NSW, as it has already been mentioned, the electronic boards are monitored through SCA ASIC which is also responsible for control distribution. Thus, the design file that was needed

[1] The XML abbreviation stands for, Extensible Markup Language. As is name suggests, is a markup language and a file format used for storing, transmitting, and reconstructing arbitrary data.

for the middleware software ought to contain the description of each board's SCA including their connections. It is quite easy for someone to guess that the boards belonging to a specific sector, for each detector technology must be grouped together. Therefore, it was imperative to build 64[2] design files "describing" the SCAs in order to generate the corresponding SCA OPC UA servers.

```
1  <SCA address="netio-next://fid/0x16b05000003f8000/0x16b05000003f0000"
2  name="MM-A/V0/SCA/L1DDC/S0/L0/E"
3  idConstraint="dont_care"
4  recoveryActionScaStayedPowered="do_nothing"
   ↪ recoveryActionScaWasRepowered="reset_and_configure"
   ↪ managementFromAddressSpace="only_if_kaputt" >
5  <CalculatedVariable name="constant_1V5" value="0.0" />
6  <CalculatedVariable name="constant_2V5" value="0.0" />
7  &SCA_L1DDC;
8  </SCA>
9
10 <SCA address="netio-next://fid/0x16b0500000088000/0x16b0500000080000"
11 name="MM-A/V0/SCA/ADDC/S0/L0/E"
12 idConstraint="dont_care"
13 recoveryActionScaStayedPowered="do_nothing"
   ↪ recoveryActionScaWasRepowered="reset_and_configure"
   ↪ managementFromAddressSpace="only_if_kaputt" >
14 <CalculatedVariable name="constant_1V5" value="0.0" />
15 <CalculatedVariable name="constant_2V5" value="0.0" />
16 &SCA_ADDC;
17 </SCA>
18
19 <SCA address="netio-next://fid/0x16b0500000008000/0x16b0500000000000"
20 name="MM-A/V0/SCA/Strip/S0/L0/R0"
21 idConstraint="dont_care"
22 recoveryActionScaStayedPowered="do_nothing"
   ↪ recoveryActionScaWasRepowered="reset_and_configure"
   ↪ managementFromAddressSpace="only_if_kaputt" >
23 <CalculatedVariable name="constant_1V2D" value="0.0" />
24 <CalculatedVariable name="constant_1V3" value="0.0" />
25 <CalculatedVariable name="constant_1V3E" value="0.0" />
26 &SCA_MMFE8;
27 </SCA>
```

Listing 1: An example of SCA object.

A small part of a XML file can be found above as an example of its structure. There are three boards (elements) that are being described. The first one is defined in lines 1 to 8 and corresponds to an L1DDC, the second one is defined in lines 10 and 17 and corresponds to an ADDC and the third one is defined in lines 19 and 27 and corresponds to an MMFE8. The creation of those XML files can

[2]The number 64 results from the fact that there are 16 sectors per side (A & C) and each detector technology needs its own XML file.

be succeded through a tool (python API) that is called "NswXmlGenerator", developed by Polyneikis Tzanis [36].

When the integration of NSW in the ATLAS cavern completed, a period of extensive debugging followed in order to make the detector operatable both standalone and as a part of the ATLAS detector. In order to achieve this, the DAQ team needed to exclude (and of course re-include) great amount of boards. Due to the aforementioned, three scripts were developed and added under "NswXmlGenerator" in order to fulfil the arised needs.

The first script, is called `commentUncommentScaDevices.py` and as its name suggests, it comments in or out the desired board providing its name or the unique hex FELIX ID RX/TX and of course the XML file name. An example of the FELIX ID RX/TX values can be found on lines 1, 10 and 19 of listing 1. The second script is called `findCommentdedDevicesFromXml.py` and its goal is to extract the commented out boards from a given XML file that is passed to the script as an input. The third script is called `updateJsonFile.py` and acts on the JSON[3] structured file which contains the information of the FELIX/OPC host and port for all the sectors of the MMG and STG detectors. Script's aim is to export the boards that have been commented out on an XML file (its second argument) and add them on the dedicated section (for each sector) on the JSON file. The final contribution was performed in the heart of the tool, the `generateXML.py`, which was tweaked accordingly so as to produce the XML files (for each sector) directly including the disabled boards, by using the optional parameter "–disabled".

5.4 Enabling/Disabling boards on DCS

The actions of the DAQ team on the XML files, had an impact on the FSM of MMGs and STGs. In the sense that disabling a board on the XML file, will make it appear offline on the DCS, propagating "NOT_READY" status on the layer (top node) that belongs. Therefore, it is important when a board is disabled in the XML file, to also disable the corresponding node from the FSM, in order to prevent the wrong propagation of state and status. The opposite action should also be taken, when a board is enabled in the XML file, the corresponding node in FSM should also be enabled so the monitoring is restored.

In order to cope with the regular changes and prevent possible mistakes from manual actions, a dedicated panel automating the procedure was created. The picture 5.3 depicts the user interface of the aforementioned panel. Through the panel, users are able to choose the sector and the side on which changes have taken place and to list the boards that have been disabled in the XML file, on the left table, while on the right one list the boards that have been disabled in the FSM. On the bottom-left part of the panel, there is a button that checks whether the boards on the left table (XML file) are the same with the ones on the right table (FSM). Depending on the outcome, which appears as message below the buttons, actions can be taken to either enable or disable the boards on the FSM (apply button).

[3] JSON stands for JavaScript Object Notation and is an open standard file format for sharing data that uses human-readable text to store and transmit data.

The panel also gives the ability to check all sectors on a side (A or C), specified by the user and to take actions, on the bottom right part.

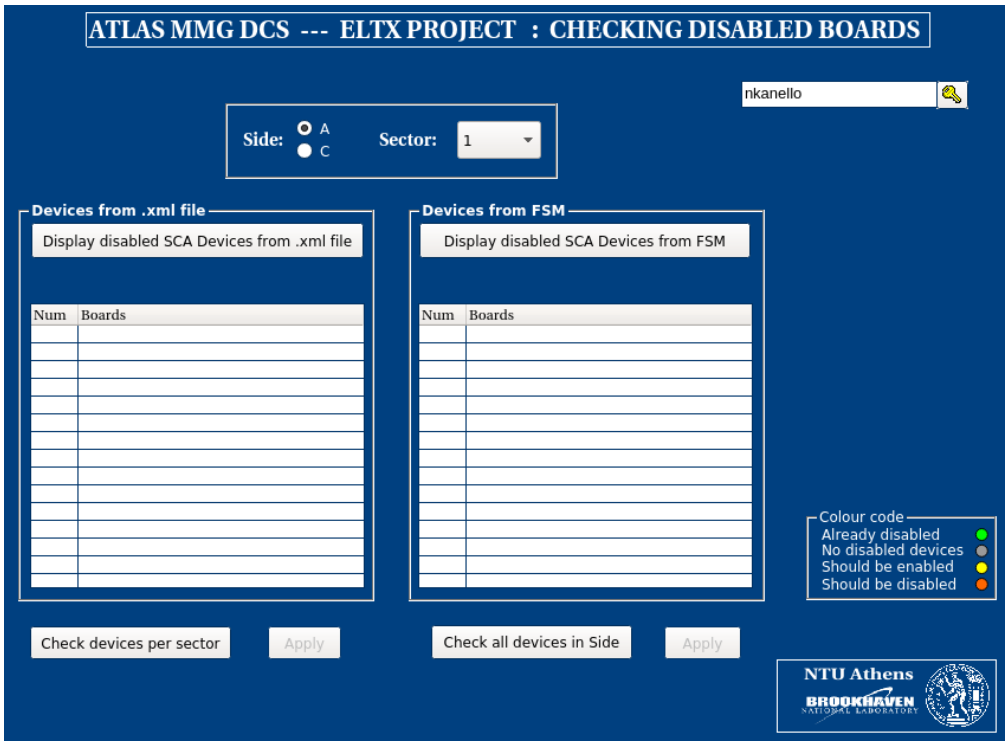

Figure 5.3: A picture of the panel that handles the enabling/disabling of the corresponding SCA boards.

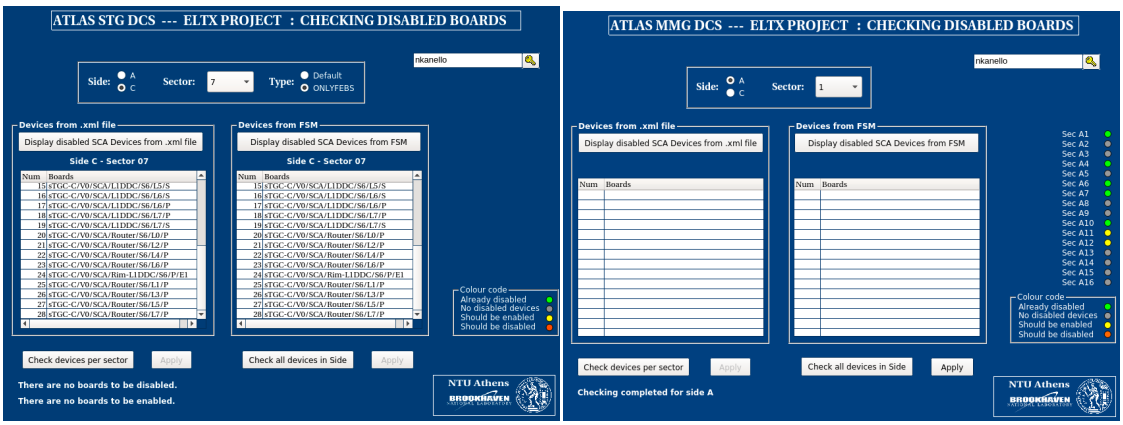

(a) Performing checks on a sector.

(b) Performing checks on side A.

Figure 5.4: Use of the panel that handles the enabling/disabling of the boards.

5.5 SCA colormap

Should one navigate deeper into electronics FSM, will find dedicated information for each board (fig. 5.5), such as its name, the OPC UA server that is connected and the status of the connection, to mention a few. In addition, there is also an illustration, showing the real view of the board with its components (ASICs) and the temperatures or the voltages, depending on the component. Having knowledge of the aforementioned parameters, is of great importance since they can ensure the good operation of the boards and therefore of the detector itself.

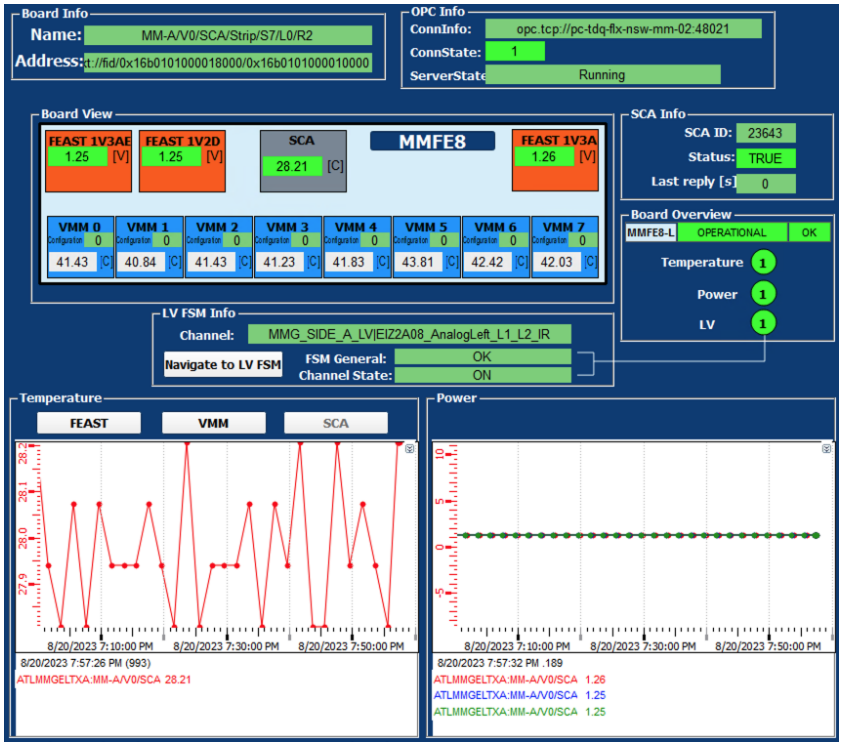

Figure 5.5: Board's view in electronic's FSM.

With all the above in mind, it was considered quite useful, for both users and detector experts, to have a dedicated (expert) panel, showing the SCAs temperatures of all boards on a layer at once, converting the values into a colour code, a *colormap*.

In figure 5.6a is depicted the user interface of the panel. Each box corresponds to the SCA's temperature of the board and they are positioned in the same way as on the detector. The "translation" of numbers into colours is performed by a dedicated function that takes as input the minimum and maximum value in a layer. The minimum value corresponds to blue colour while the maximum to red and the intermediate colours are created through the function.

Users are given the ability to choose the side, that they want to be displayed, the layer and also the minimum and maximum displayed value of temperature. Apart from that, it was also considered use-

ful to visualise the status of the SCAs (fig. 5.6b) within the same panel, using the corresponding option on the top right.

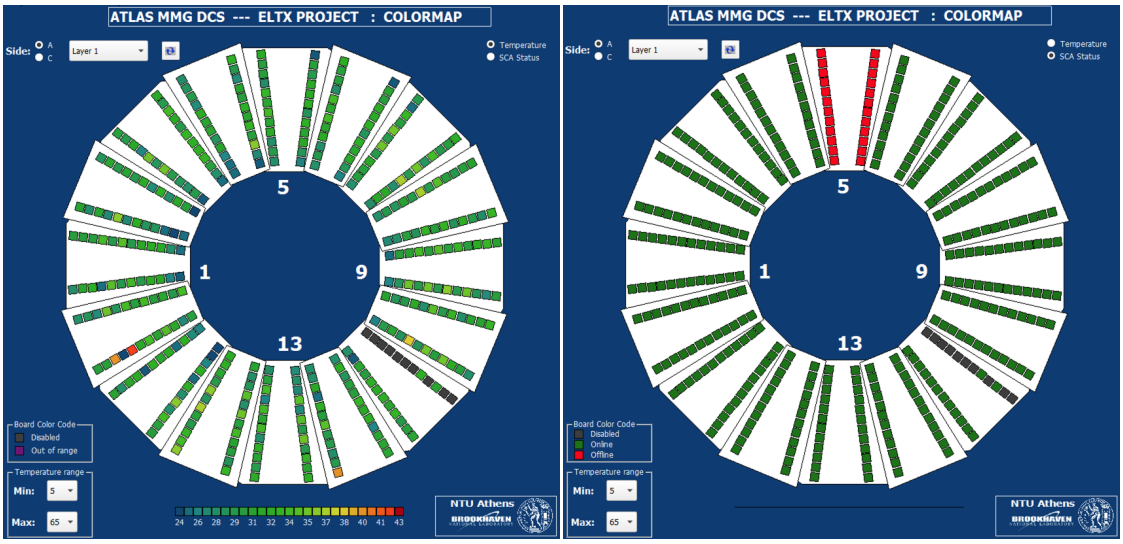

(a) A snapshot of SCAs temperatures on layer 1.

(b) A snapshot of SCAs status on layer 1.

Figure 5.6: SCAs colormap panel.

5.6 Electronic's FSM

Near the end of each year there is a dedicated period of time, the so called YETS[4], that the LHC stops its operation and maintenance on experiments takes place. DCS plays a crucial role, even in that period, in monitoring and controlling the subsystems, since interventions might require specific actions on their services like powering off and on the high voltage (of detectors) or the low voltage (of electronics) etc.

During YETS of 2023, it was observed that the FSM of electronics on MMGs was frozen when powering on or off the low voltage on the whole wheel (either A or C side). As a result the state and status propagation of its components stopped. An investigation of the project started, shortly after, in order to understand and eventually fix the origin of the problem.

Electronics' project monitors and controls a great amount of low-level parameters, which apparently consume a lot of resources. During the investigation, it was found out that two scripts, that are running constantly on the background (as managers) and consequently might affect the propagation problem, could be written in a more efficient way.

The first one was the `mmgEltx_copyMechanismForLVState.ctl`. In order to calculate the state of a board, it is also essential to know the state of the low voltage channel that is powering the specific

[4]YETS acronym stands for Year-End Technical Stop.

board. Consequently, a script that copies the states of low voltage channels (whenever they change) was imperative to be created. As its name suggests, the script connect to low voltage project and copies the state of each channel to a local datapoint element (lvFsmState). What was changed is the way the script is connected to each datapoint element of the low voltage project, in order to get its state and store it into the local DPE. The connection is achieved through a dedicated function of WinCC OA which is called `dpConnect()`. Initially this was done directly on the 320 channels of the project. Now the connection is being made on the channels of each sector separately.

The second script was the `mmgEltx_LvToScaAffection.ctl`. Its purpose is to activate or deactivate the alarm of SCA's DPE ".online", depending on low voltage channel's state. Each low voltage channel is connected to eight front-end boards. Therefore, when the status of a low voltage channel is changed, the script should act on its eight boards. Originally, the script used two mappings, the first one stored the names of the boards (ex.: `MM-A/V0/SCA/Strip/S0/L0/R0`) as keys and their corresponding channels (ex.: `MMG_SIDE_A_LV_EIZ3A15_AnalogRight_L3_L4_IR`) as values. The second mapping stored the low voltage channels as keys and the corresponding (eight) boards as values. However, the use of mappings is not considered optimal when they are accessed serially [37] and their replacement is considered imperative. In the new approach, the associated boards are found when the state of a low voltage channel is changed and the actions on alarms follow.

5.7 Round trip time parameter

Developments are in progress in multiple levels of NSW in order to ensure the stable operation of the detector. One of them is the SCA OPC UA server that is still updated. One of its latest updates is the inclusion of round trip time (RTT) parameter. The round trip time is defined as the amount of time it takes for a signal to be sent, from one endpoint to another, and received. In NSW's case the first endpoint is OPC UA server and the other is FELIX.

The inclusion of RTT parameter into OPC UA server should also be reflected into DCS and more specifically into WinCC OA. It was decided to follow the "formal" way and perform the inclusion by updating the `fwSca`. The `fwSca` is one of the general frameworks that is used by all ATLAS subsystems. Thus, it was considered better to make a general work so the other subsystems could be also benefit.

The update of `fwSca` was performed using `Cacophony` [38], a quasar extension module that helps with integration of quasar-made OPC-UA servers into WinCC OA. The first thing that had to be done was to clone the latest version of SCA OPC UA server [39], then to clone `Cacophony` inside the file of the server and run the python script `generateStuff.py` in order to produce the three new control scripts of `fwSca`. After the successful creation of the new `fwSca`, some important modifications of the source code were performed to ensure the correct integration of the new parameter, without creating problem to the already existing ones. The new version of framework underwent review by Central DCS and more specifically by Paris Moschovakos, in order to validate its correctness before its release. A test followed on the electronics (ELTX) project of MMGs side A, in order to verify that the new

`fwSca` works as expected. In this test, after the installation of the framework, it was confirmed that the RTT has been added in boards' (DPEs) parameters without interfering with the existing ones.

After the new framework was successfully validated, the necessary changes had to be performed to the panels configuring the low-level parameters of WinCC OA (DPEs). These changes were required to include the RTT parameter, set the descriptions, and enable archiving. The panels that have been modified to meet the needs are,

1. `mmgEltx_fwSca_dpCreation.pnl`
2. `mmgEltx_descriptionHandling.pnl` and
3. `mmgEltx_archiving.pnl`

5.8 Beam Injection System Logviewer

The operation of LHC is a quite complex and sophisticated procedure in order to reach the collisions that will eventually give the desired data for analysis. In general, three different types of modes are defined: the accelerator mode, that provides a summary of the LHC machine state (shutdown, beam setup, proton physic, etc), the beam mode, that provides a description of the main phases of the accelerator cycle (setup, injection probe beam, stable beams) and finally the sector operation mode that provides a binary flag per LHC sector to define whether or not it is operational [40].

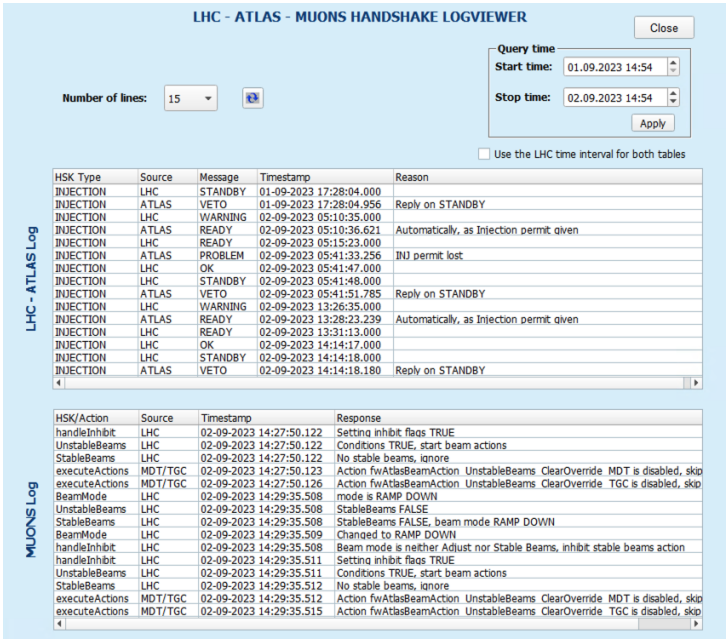

Figure 5.7: The user interface of muon beam injection system logviewer.

Every LHC cycle is a sequence of tightly coupled tasks that need to be carried out in strict order and have to be accomplished successfully, in order to allow the LHC machine to make a transition from one state to another. The sequence execution is done by a high level software application called the LHC Sequencer. In each transition, a handshake among LHC and the experiments is mandatory in order to continue the sequence. For example, when the LHC "asks" for injection permit, then ATLAS should be in safe state in order to "perform" the handshake.

The signals needed for the aforementioned procedures are handled by the beam injection system (BIS) interface. For muon sub-systems it was considered useful to develop a dedicated user interface, displaying the handshakes between the LHC and the ATLAS (top table on fig. 5.7) as well as the reactions of MMGs, STGs, MDTs and TGCs (bottom table on fig. 5.7). The handshakes between the LHC and the ATLAS are taken from a dedicated datapoint element that has been created from Central DCS for another user interface. The messages of muon sub-systems are taken directly from the scripts that control their behaviour and are written into a dedicated datapoint element. All messages are archived in order to be accessed, if needed, later in time.

Through the panel, users are given the ability to choose the number of lines that are displayed in tables. Moreover, users are able to set the start and end time of their choice. When the panel is called, it sets by default as end time, the time that has been invoked and as start time exactly 24 hours before the end time. Finally, because the messages of muon sub-systems are far more, compared to the ones of LHC and ATLAS handshakes, a button has been added to display all the messages (independently of the number of displayed messages) from muon sub-systems in the time window defined by the user.

Part III

DETECTOR PERFORMANCE STUDIES

6 Interactions of particles with matter

It has been known that particles and radiation in general, are being detected through their interaction with the medium they "penetrate". Based on the interaction(s), scientists are able to identify and categorise them.

6.1 Energy deposition of charged particles in matter

The interaction of charged particles with matter is governed by electromagnetic processes. A charged particle, entering any absorbing medium interacts with the shell electrons that are on its trajectory. Depending on the energy of the particle and the distance from medium's molecules/ atoms, their electrons might occupy a higher energy layer (excitation) or being completely released (ionisation). Moreover, charged particles, can be detected through the emission of electromagnetic radiation like bremsstrahlung, Cherenkov or transition radiation.

During each interaction, particles lose a small fraction of their initial energy until they are finally stopped. The average distance a particle travels before changing its direction or its energy, is called *mean free path* of a particle and is defined as,

$$\lambda = \frac{1}{\mu} = \frac{1}{n\sigma} \tag{6.1}$$

where n is the density of particles in the medium (electrons in our case) and σ is the cross-section, a measure for the probability of a reaction. The inverse of *mean free path*, $1/\lambda$, is the the number of primary ion pairs per unit length and depends on the type of charge particle, its velocity and the gas mixture [41].

The interactions are purely random and thus they are governed by statistics. The probability of having k ionisation interactions over a given distance x follows the Poisson distribution,

$$P\left(k; \frac{x}{\lambda}\right) = \frac{\left(\frac{x}{\lambda}\right)^k}{k!} \exp\left(-\frac{x}{\lambda}\right) \tag{6.2}$$

The *mean energy loss* (which is also called *stopping power*) per distance of charged particles, apart from electrons and positrons[1], is described by *Bethe & Bloch* formula,

$$-\left\langle \frac{\mathrm{d}E}{\mathrm{d}x} \right\rangle = K\frac{Z}{A}\frac{z^2}{\beta^2}\left[\frac{1}{2}ln\left(\frac{2m_e c^2\beta^2\gamma^2 T_{max}}{I^2}\right) - \beta^2 - \frac{\delta(\beta\gamma)}{2} - \frac{C(\beta\gamma, I)}{Z}\right] \tag{6.3}$$

where,

$K = 4\pi r_e^2 m_e N_A c^2$

Z, A are the atomic number and the atomic weight of the medium

z, β are the charge and velocity of the incident particle

m_e is the electron mass

γ is the Lorentz factor

T_{max} is the maximum kinetic energy transferable to an electron in an elastic collision

I is the mean excitation energy (characteristic of the absorber medium)

$\delta/2$ is the so-called density correction term for high energies

C/Z is the shell correction term for low energies

Interpreting the formula one can observe that there is strong dependence on the atomic number of the absorbing material as well as to the square of the charge of the incident particle. At low kinetic energies ($\beta\gamma \leq 1$), a dominance of the $1/\beta^2$ is observed which is explained by the fact that, the momentum transfer increases with the effective interaction time. While energy is increased, there is a broad minimum, around $\beta\gamma \approx 3 - 3.5$ (fig. 6.1). Particles with a momentum in that region are called, *minimum-ionising particles* (*mips*). At high kinetic energies the dominant term is $\ln\gamma$. This is due to the asymptotic increase of the maximum energy transfer T_{max} with γ, which is a purely kinematic effect and because of the increasing transverse extension of the electric field with γ, a relativistic effect.

6.1.1 Energy deposition of electrons and positrons

As it has already been mentioned, the aforementioned do not constitute the full "picture" for electrons and positrons, since photon radiation (bremsstrahlung) becomes relevant already at small energies due to their small mass. Additionally, energy loss resulting from ionisation varies in comparison to heavy charged particles due to differences in kinematics, spin, and their identical (or opposite for positrons) properties when interacting with the medium's electrons.

[1] that their energy loss is slightly different due to their small mass

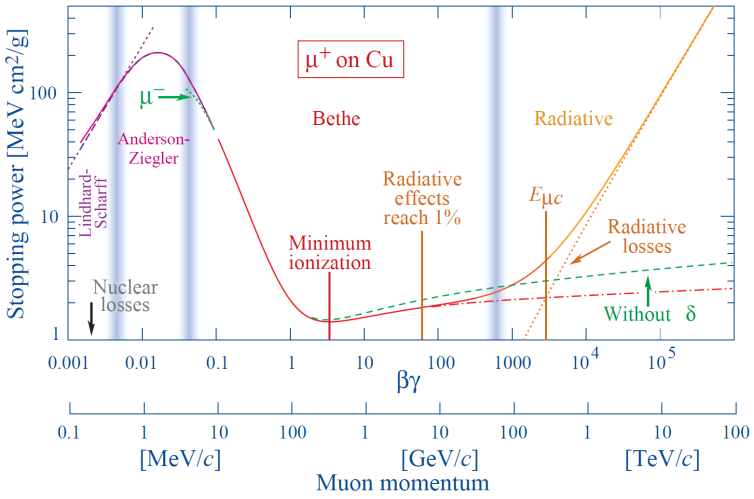

Figure 6.1: Stopping power for different particle energies. The red curve (on central part) is described by Bethe & Bloch formula [42].

6.1.2 Energy deposition of photons

Photons, interact with matter mainly with the following mechanisms, (i) photoelectric effect (ii) Compton effect and (iii) pair production. In photoelectric effect, a photon transfers its *total* energy to an atom which emits a shell electron[2] (also known as photoelectrons). This process creates a vacancy that is filled either by a free electron of the medium or by the re-arrangement of atom's electrons from other shells. In the latter case, an x-ray photon is emitted which most probably will be reabsorbed near the photoelectric effect [43].

In Compton effect, a photon is scattered off a free of quasi-free[3] electron. When an electron is also "kicked-out" of the atom, carrying the recoil momentum, then the process is called Compton scattering. Using the equations of energy and momentum conservation, one can calculate the energy of the scattered photon as a function of its scattering angle (θ),

$$h\nu' = \left[h\nu \Big/ \left(1 + \frac{h\nu}{m_0 c^2}\right)\right](1 - \cos\theta) \tag{6.4}$$

It is also possible, in the presence of a Coulomb field, a photon to be converted into an electron-positron pair, if its energy is greater than twice the rest mass of the electron (≈ 1.02 MeV).

In the sub-MeV range, the photoelectric effect prevails, and its likelihood diminishes as the photon's energy increases. The Compton scattering process becomes significant when encountering photon energies in the range of a few MeV. However, for energies exceeding 10 MeV, photons predominantly interact with matter through pair-production mechanism.

[2] The interaction cannot occur with free electrons.

[3] A shell electron is termed "quasi-free" when its binding energy is much less than the energy of incoming photon ($E_B \ll E_\gamma$).

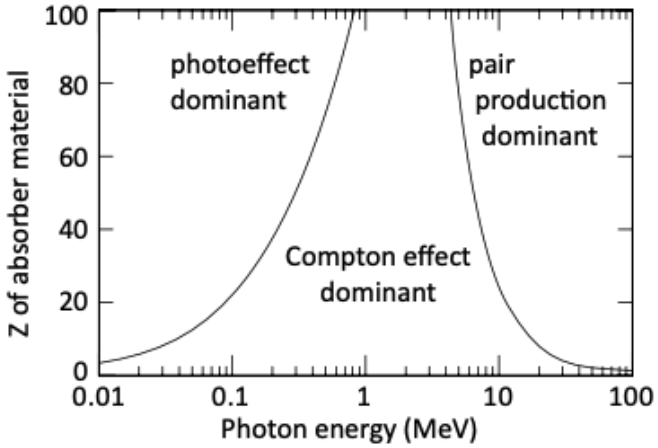

Figure 6.2: Dominant photon interactions with matter as function of energy.

6.2 Movement of charge carriers

Detection techniques for charged particles commonly rely on ionisation of sensitive detector's medium through their passage. Applying an electric field, the created charges move toward the electrodes which sense the signals induced by this movement. The microscopic position and velocity of distributions of charge carriers in a medium, depend on external forces, like the ones from electric and magnetic field, and other parameters like temperature and pressure and they are described by Boltzmann's transport equation. The drift velocity $\mathbf{u}_D$ is defined as the mean value of the velocity vectors of particle collection, with respect to the distribution function f.

$$\mathbf{u}_D =< \mathbf{u} >= \int \mathbf{u} f(\mathbf{u}) \ \mathrm{d}^3\mathbf{u} \tag{6.5}$$

Based on the nature of particles (electrons, ions, etc..) and the conditions applied to them, the aforementioned equation yields different results. The present thesis examines the case of gaseous detectors, therefore the results of ion and electron movement will be discussed.

6.2.1 Drift and diffusion in gases

In the absence of electric field, both electrons and ions, that have been created by the ionisation process, start losing their energy due to multiple collisions with atoms and molecules of a gas. Due to this rapid energy loss, both electrons and ions, acquire the thermal energy distribution of the medium. Their properties can be described by the classic kinetic theory of gases, since both behave as neutral molecules in the process of ionisation [44]. The probability of an atom or molecule to have energy ε at the absolute temperature T follows the Maxwell - Boltzmann law,

$$F(\varepsilon) = 2\sqrt{\frac{\varepsilon}{\pi(kT)^3}} \exp\left(-\frac{\varepsilon}{kT}\right) \tag{6.6}$$

where k is Boltzmann's constant. Integrating the previous equation over the distribution, the average thermal energy is given by,

$$\bar{\varepsilon} = kT \tag{6.7}$$

Two of the most fundamental properties of electrons and ions in gases are their *drift velocity* and *diffusion*. The knowledge of them contributes to the understanding of the operational characteristics and performance of gaseous detectors. The corresponding distribution of velocity v for a particle of mass m is given by the expression,

$$f(v) = 4\pi\left(\frac{m}{2\pi k_B T}\right)^{3/2} v^2 \exp\left(-\frac{mv^2}{2kT}\right) \tag{6.8}$$

Integrating again, we get the average value of the velocity can be calculated by,

$$\bar{v} = \sqrt{\frac{8kT}{\pi m}} \tag{6.9}$$

The diffusion of locally produced electrons and ions correspond to a Gaussian distribution,

$$\frac{\mathrm{d}N}{N} = \frac{1}{\sqrt{4\pi Dt}} \exp\left(-\frac{x^2}{4Dt}\right) \mathrm{d}x \tag{6.10}$$

where, $\mathrm{d}N/N$ is the fraction of the charge which is found in the length element $\mathrm{d}x$ at a distance x after time t and D is the diffusion coefficient.

6.2.2 Ion mobility and diffusion in electric field

When an electric field is applied in the gas volume, a net movement of ions, along the field direction is superimposed over the statistically disordered motion. The average velocity is linearly proportional to the electric field and is given by the expression,

$$v_d^{ion} = \left(\frac{1}{m+M}\right)^{1/2} \left(\frac{1}{3kT}\right)^{1/2} \left(\frac{eE}{N\sigma}\right) = \mu E \tag{6.11}$$

where, m is the mass of ion, M the mass of the gas molecule, k Boltzmann's constant, T the temperature, N the density number and σ the scattering cross-section of ions by gas molecules. The quantity μ is defined as the *ion mobility* and is specific to the type of ion, moving in a given gas, depending on pressure and temperature.

$$\mu(P,T) = \frac{T}{T_0}\frac{P_0}{P}\mu(P_0,T_0) \tag{6.12}$$

Studies have shown that ions' mobility remains constant up to very high electric fields, due to the fact that their average energy is almost the same. In case of a gas mixture, the ion mobility can be calculated through Blanc's law,

$$\frac{1}{\mu} = \sum_i \frac{f_i}{\mu_i} \tag{6.13}$$

where the coefficient f_i gives the fraction of the specific gas in the mixture and μ_i denotes the ion mobility in the corresponding gas. Concerning diffusion, in the presence of electric field, diffusion coefficient D is directly related to the ion mobility through the Nernst - Townsend - Einstein formula,

$$\frac{D}{\mu} = \frac{kT}{e} \tag{6.14}$$

6.2.3 Electrons mobility and diffusion in electric field

Electrons, under the presence of an electric field in the gas, drift in opposite direction to the field's vector. Their drift velocity can be deduced in similar way as in the case of ions and is given by the Townsend formulation,

$$v_d^e = k\frac{eE}{m}\tau \tag{6.15}$$

where τ is the mean time between collisions and k is a constant with value between 0.75 and 1, depending on assumptions about the energy distribution of electrons. Although, Townsend's formulation is a convenient way for qualitative evaluations, it is not very practical owning to the dependance of drift velocity and τ on the nature of gas and on electric field.

However, the problem of electrons' drift inside a gas medium can also be approached classically. The equation of motion of an electron with mass m, within a gas, subjected to both an electric field $\mathbf{E}$ and magnetic field $\mathbf{B}$, is given by the equation,

$$m\frac{\mathrm{d}\mathbf{v}_d^e}{\mathrm{d}t} = e(\mathbf{E} + \mathbf{v}_d^e \times \mathbf{B}) - \frac{m}{\tau}\mathbf{v}_d^e \tag{6.16}$$

where the term $\frac{m}{\tau}\mathbf{v}_d^e$, is the friction force. Assuming that an electron drifts with constant velocity *only* under a uniform electric field the equation 6.16 is simplified into,

$$|\mathbf{v}_d^e| = \frac{eE}{m}\tau \tag{6.17}$$

which is in good agreement with the equation 6.15 for the case of $k = 1$. The same diffusion laws that describe ions, apply also for electrons, spreading the initially localised charge cloud, but with rather increased diffusion coefficient due to their smaller mass. The length of diffusion depends on the gas as well as the intensity of electric field E, owning to the increase of the electron energy. In order to take the aforementioned into account, the expression 6.14 can be modified, introducing a phenomenological quantity ϵ_k, which is called characteristic energy,

$$\frac{D}{\mu} = \frac{\epsilon_k}{e} \tag{6.18}$$

The characteristic energy for thermal electrons is $\epsilon_k = kT$, reducing to 6.14. It is also important to mention that the mobility of electrons, is not constant apart from very weak electric fields. This stems from the small mass of electrons that allows to them the substantial increase of their energy between collisions.

6.3 Avalanche formation

In the presence of strong electric field, the electrons that have been created by the ionisation process (?) can gain sufficient kinetic energy in order to further ionise neutral gas atoms or molecules, producing secondary ionisations. The same process also affects the secondary electrons, that eventually create higher order ionisations contributing in a multiplication that takes the form of a cascade which is known as Townsend avalanche [45]. The avalanche forms a drop-like shape because electrons, which dominate in the head of the drop, drift faster than ions, which make up the tail. This multiplication process is important in order to have a reliably detected signal of singly charged particles, since the ionisation charge of minimum ionising particles in gas detectors is typically only 100 e/cm.

The quantity of secondary ion pairs generated per unit of length of drift, corresponds to a multiplication factor known as the *first Townsend coefficient* and is given by the expression,

$$\alpha(E, \rho) = 1/\lambda \tag{6.19}$$

where λ is the mean free path of the ionisation electron, defined in equation, 6.1. The coefficient is a function of the electric field E and the gas density.

Assuming that n_0 electrons enter the electric field region, the total number of electrons after a distance dx is given by the expression,

$$\mathrm{d}n = n\alpha\,\mathrm{d}x \Rightarrow n(x) = n_0 \exp(\alpha x) \tag{6.20}$$

Moreover, there is a definition between the initial and final number of electrons called gas gain, given by expression,

$$G = \frac{n}{n_0} \tag{6.21}$$

6.4 Signal formation

It is well known that the electron-ion pairs produced within a gaseous detector by ionising events, drift towards anode and cathode, respectively, under the effect of the applied electric field. During the drift, induced signals appear on the electrodes, with polarity and time structure that depend on the counter geometry, field strength and mobility of the charges. It is worth noting that charge does not need to reach the electrode for signal generation. The calculation of induced signals can be performed through the Shockley–Ramo theorem [46, 47] which states that the instantaneous current I induced on a given electrode due to the motion of a charge q is given by the expression,

$$I = E_u q u \tag{6.22}$$

where u is the drift velocity and E_u is the component of the electric field in the direction of u. Taking into account all charges, in the current density term $J(x,t)$ the expression takes the following form [48],

$$I = -\frac{1}{V} \int \mathbf{J}(x,t) \cdot \mathbf{E}(x,t) \, \mathrm{d}^3 x \tag{6.23}$$

7 Study of MM in a high radiation environment

7.1 Gamma Irradiation Facility ++

The Gamma Irradiation Facility (GIF++) is a collaborative project among CERN's departments, which offers the necessary infrastructure to research teams, for conducting studies on detectors already in use at CERN and also on emerging technologies. As it has already been mentioned high-luminosity LHC (HL-LHC) upgrade sets a new challenge for particle detector technologies. Detailed insight into detector performance under high particle flux, as well as thorough comprehension of potential aging effects due to continuous particle bombardment, play a crucial role in achieving an optimised design and efficient operational mode. Therefore, the infrastructure of GIF++, focusing on the characterisation and understanding of large particle detectors, provides a 14 TBq ^{137}Cs source along with high energy charged particle beams coming from the secondary SPS beam line H4 in EHN1 (887). The momentum range of the beam line varies from 10 GeV up to 450 GeV, the maximum SPS momentum [49].

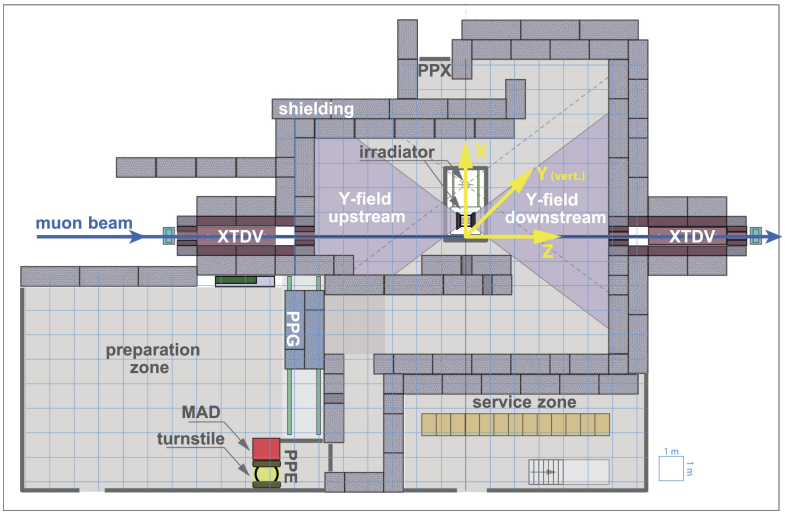

Figure 7.1: Layout of GIF++ facility [50].

Therefore, researchers are able to recreate the conditions that the detectors are going to face in the ATLAS cavern and of course, even create more hostile environments pushing detectors limits. Since

the source of ^{137}Cs emits constantly photons, the simulation of different background conditions is made through a set of Lead filters attenuating appropriately the photon flux. Moreover, research teams can take advantage of the 100 m^2 irradiation bunker with its two independent irradiation zones, upstream and downstream, (fig. 7.1) placing their detector under test (DUT) at the desired place according to their needs.

7.2 Testbeam periods

Generally, a thorough investigation and characterisation of a detector's properties are necessary before its use in experiments. That is the reason that research teams participate in a numerous (two-week) testbeam periods, through out the year, in facilities like GIF++, in order to test their setups. Resistive Micromegas have been tested for many years in testbeam periods, at different facilities and continue to be tested until today.

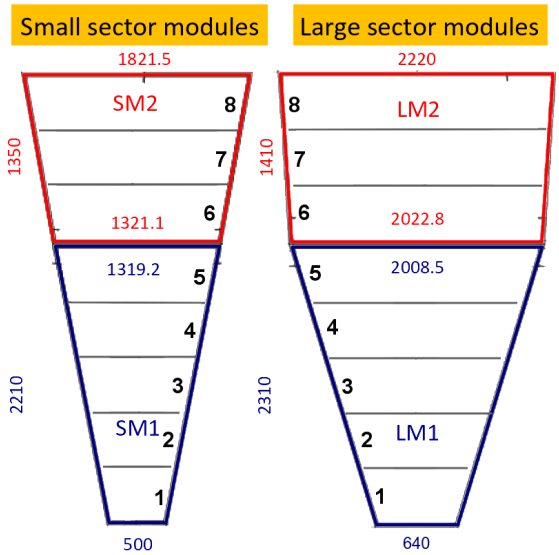

Figure 7.2: Schematic representation of Micromegas sector modules [51].

In the following paragraphs, the focus will be on the testbeam periods in July and October of 2022, both conducted at the GIF++ facility. In July's testbeam, the detector under testing was the SM1 module (figure 7.2). Out of the five PCBs, only PCB 3 was used since it was the one that the beam was crossing. Additionally, an external reference track provided by four smaller Micromegas detectors, named BeamLine (BL), each with an active area of 40 × 40 cm^2. Part of the setup can be found on figure 7.3.

Significant data was accumulated for a wide range of experimental parameters. The main parameters under testing were (i) the high voltage of amplification gap[1], starting at 490 V up to 530 V (gas

[1] Attention was given in amplification gap since the optimal value for conversion/drift gap has already been found experimentally to be 240 V.

amplification), (ii) the attenuation factor of the source, taking data for all of the following numbers, 1, 2.2, 4.6, 10, 22, 46, 100, 220. An attenuation factor of 1 indicates that the source is not attenuated (fully open), while an attenuation factor of 46420 indicates complete attenuation (fully closed). (iii) the different values of VMM threshold, ×9, ×12, ×15, ×18 rms (iv) the VMM peaking time (100 ns and 200 ns) and finally, (v) for different values of gain such as, 9, 12 and 16 mV/fC.

The data collection was highly successful, accumulating all the necessary data for both vertical and inclined positions of SM1, for further analysis. Therefore, in October's testbeam period, it was decided to implement a slightly more complex setup accumulating data for the same parameter (previously mentioned). Overall, in addition to the four track reference chambers (BL) and the SM1 module, the LM2 module was added to the detectors under testing (figure 7.4).

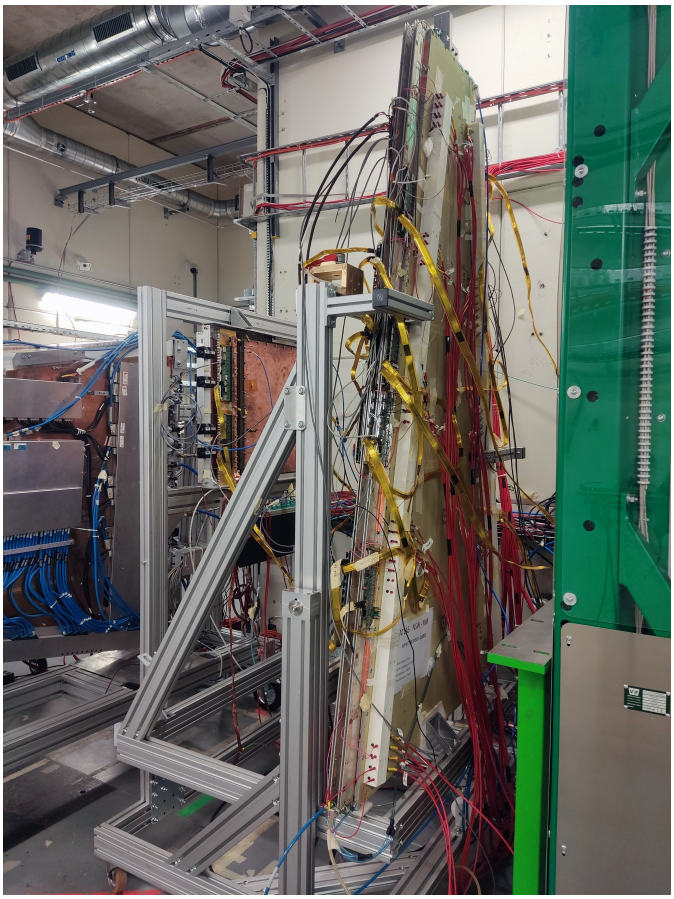

Figure 7.3: The SM1 module in front of radiator in July's testbeam period. Behind the SM1 module, are the two (out of four) tracking reference chambers.

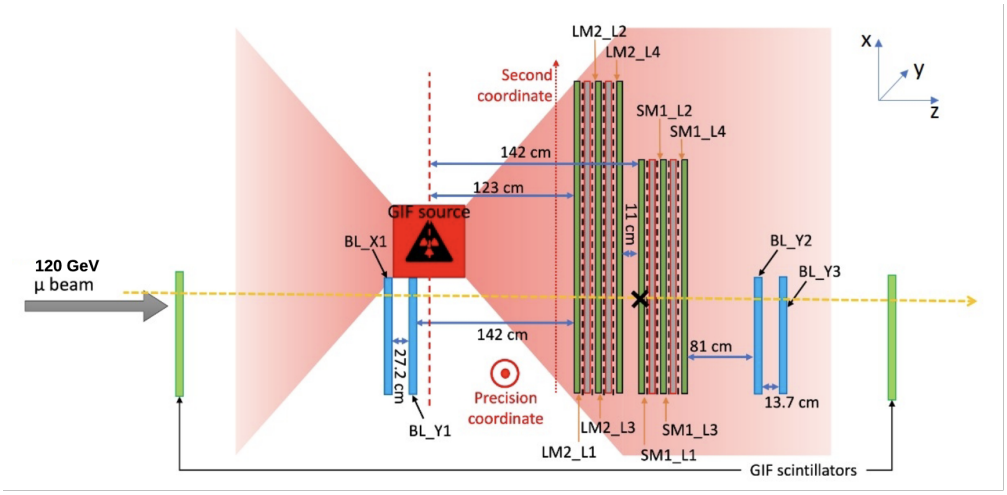

Figure 7.4: A schematic representation of setup in October's testbeam period.

7.2.1 Readout system

The readout system, in July's testbeam period, consisted of eight MMFE8s for SM1[2] and eight MMFE8s for BL chambers. These sixteen boards are connected to eight L1DDCs via twinax cables and each L1DDC is linked to a patch panel through optical fiber. The patch panel is further connected to FELIX via a long fiber, facilitating the transfer of data off-detector. FELIX is connected to ALTI, that takes the trigger signal from GIF++ scintillators, and to swROD for data processing. For more details on electronics the reader is referred to section 3.3. In October's testbeam, the readout was the same with the addition of eight MMFE8s used for the readout of LM2 module's PCB 5.

[2]Each PCB on each layer is read out by two MMFE8s

7.3 Identifying an issue

During October's testbeam period, when the first data started to be analysed an unexpected behaviour was observed on *efficiency* of detectors under test. Figure 7.5 presents the efficiency plot for each layer of SM1 and LM2 modules as a function of gamma intensity (attenuation factor). Starting from the right part of the plot, where the attenuation factor 220 is depicted, and moving to the left, a drop in efficiency is already observed at attenuation factor 10 (with half PCBs enabled for both modules). The background conditions that are created from the source when the attenuation factor is 10, are equivalent to the expected background of HL-LHC on module's PCB 1.

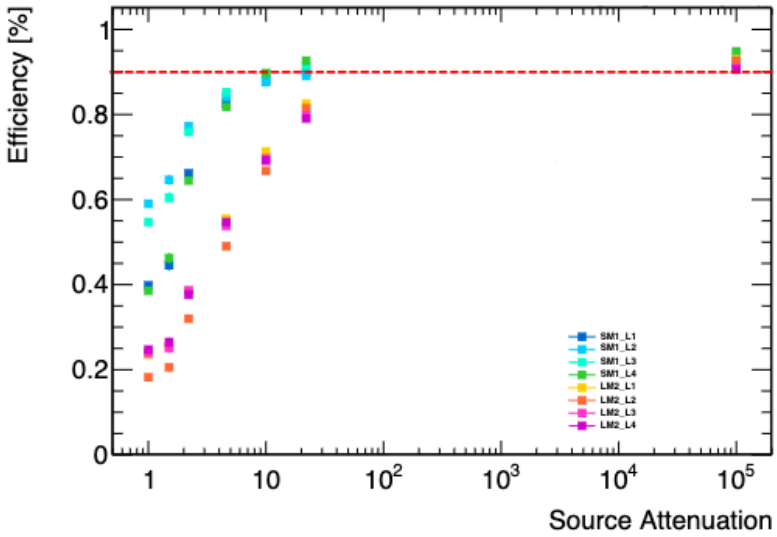

Figure 7.5: The efficiency of detectors under testing (SM1 and LM2) as a function of source attenuation (Source: Valerio D'Amico).

This drop in efficiency raised a lot of questions, with the main ones being whether it is really true and, if so, what the cause of this observation is. The investigation, in order to answer the previous questions, started from *beam profile* plots. Generally, a linear behaviour similar to the plots of attenuation factor 46 (fig. 7.6a) would be expected. Instead, in the plots of low attenuation factors, as in the case of 1, scattered points with drops were observed (fig. 7.6b). The beam profiles measured for threshold ×9 rms, peaking time 200 ns, gain 16 mV/fC and amplification gap voltage 520 V.

The search continue with the *gas gain* variation, meaning the variation of high voltage under specific gas condtions. The following plots illustrate the relationship between mean raw hits and gamma intensity of the source (attenuation factors) at 520 V and 530 V, along with the mean number of clusters and gamma intensity of the source at the same voltages. Despite the expected linear behaviour, all plots exhibit saturation as gamma intensity increases which is indicated by a trend towards the right on the x-axis. Additionally, when comparing the mean raw hits versus gamma intensity at 520 V (fig. 7.7a) with the case at 530 V (fig. 7.7c), it is evident that in the former plot the values are greater, con-

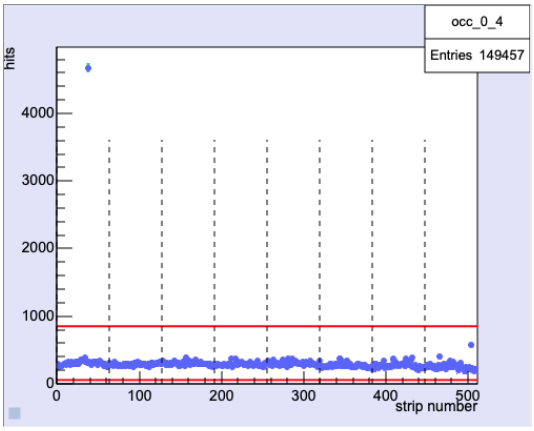

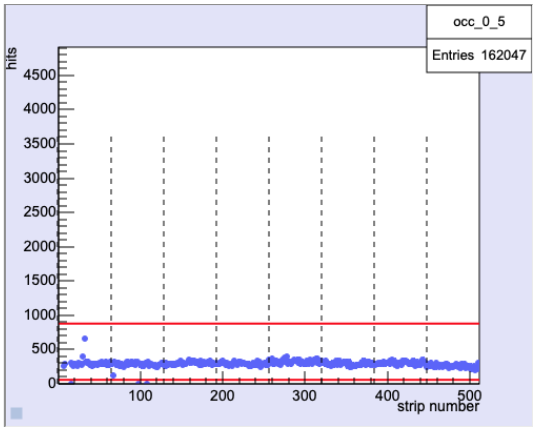

(a) Beam profile at attenuation factor 46, 520 V.

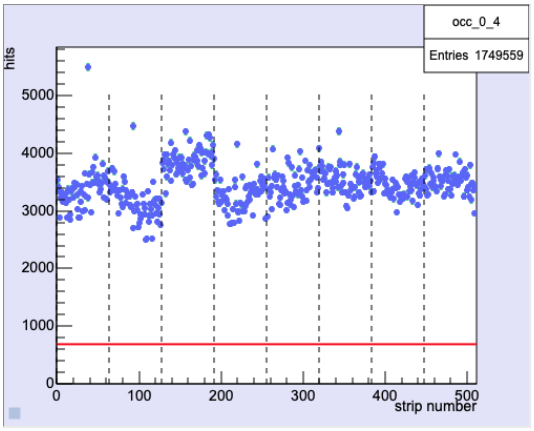

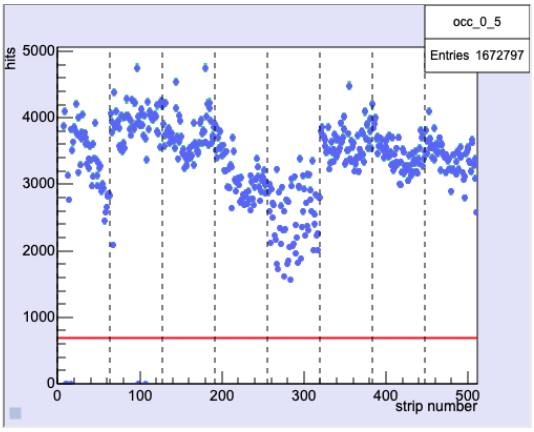

(b) Beam profile at attenuation factor 1, 520 V

Figure 7.6: Beam profile comparison at attenuation factor 1 and 46.

trary to what it was expected. The same behaviour is observed when one compares the mean number of clusters versus the gamma intensity at 520 V (fig. 7.7d) and at 530 V (fig. 7.7b).

The final part of the investigation, involved the study of *electronics gain* variation. In the following plots, one can observe the relationship of mean raw hits with the high voltage as well as the relationship of mean number of clusters with the high voltage, for the various attenuation factors. This analysis is conducted for the case of 1 mV/fC and 9 mV/fC (VMM) gain, respectively. Generally, the expected behaviour is a linear increase of both mean raw hits and mean number of clusters as the value of high voltage increases, as in the case of 1 mV/fC gain (figures, 7.8a, 7.8b). However, in the case of 9 mV/fC gain, the linearity is getting lost as the gamma intensity increases, that is for lower attenuation values like 1, 1.5 and 2.2 (figures, 7.8c, 7.8d).

All of the investigations above have led to the conclusion that the cause of all previous observations was data loss.

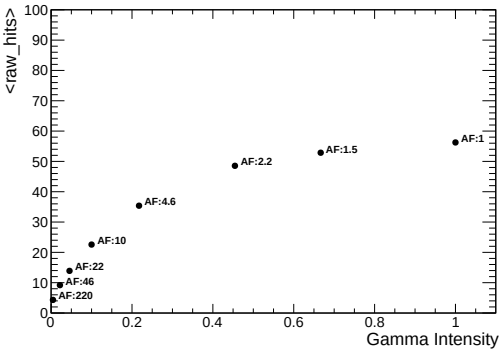

(a) Mean value of raw hits versus the gamma intensity at 530 V.

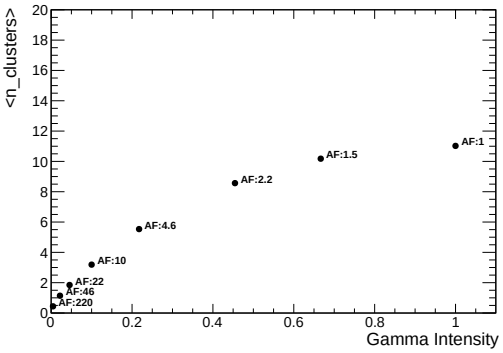

(b) Mean number of clusters versus the gamma intensity at 530 V.

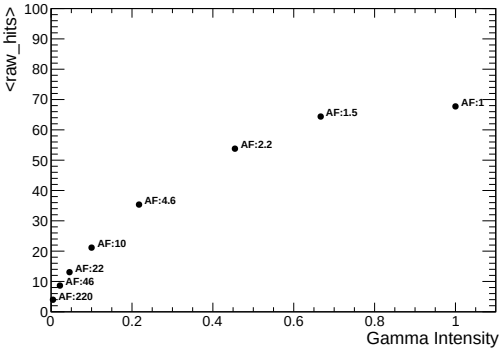

(c) Mean value of raw hits versus the gamma intensity at 520 V.

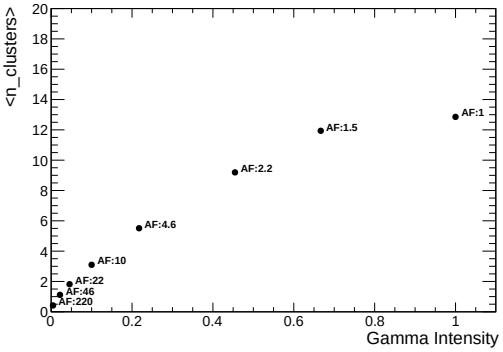

(d) Mean number of clusters versus the gamma intensity at 520 V.

Figure 7.7: Comparison of mean raw hits and mean number of clusters as a function of gamma intensity between 520 V and 530 V.

7.4 Finding a solution

The results that have been presented in the previous section, raised questions among the team about the origin of the observed data loss. As a consequence, tests outside of October's testbeam period were planned, with a far more simplified setup, in order to troubleshoot the system and find the cause of data loss.

The new setup consisted only of the SM1 chamber and the readout system reduced to only two MMFE8s, in order to narrow down its complexity. The tests began with a new firmware of FELIX, that the homonymous team created after a request. Generally, FELIX is responsible for sending the L0A signal to each VMM, in order to initiate the transmission of data to the ROC ASIC and for sending the L1A signal to the ROC, in order to start transmitting the collected data back to FELIX itself. In the current phase of data taking (Run 3), these two signals are sent at the same time, so the

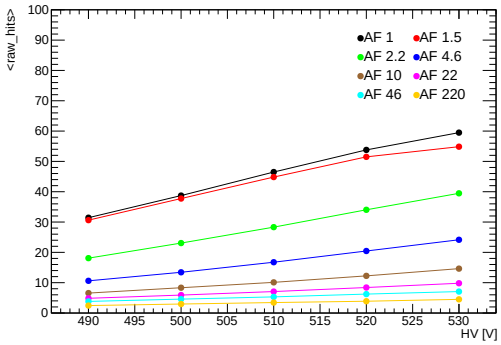

(a) Mean value of raw hits versus high voltage at 1 mV/fC gain.

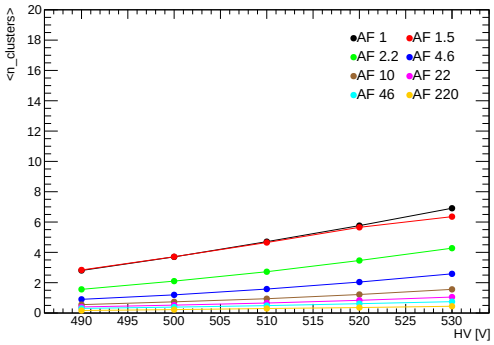

(b) Mean number of clusters versus high voltage at 1 mV/fC gain.

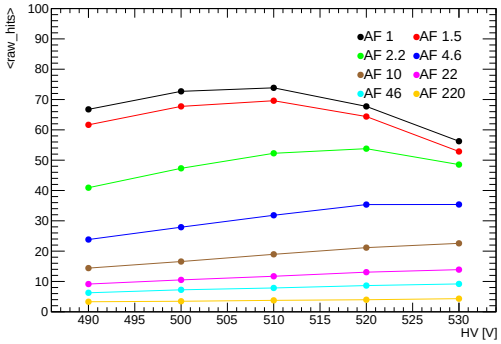

(c) Mean value of raw hits versus high voltage at 9 mV/fC gain.

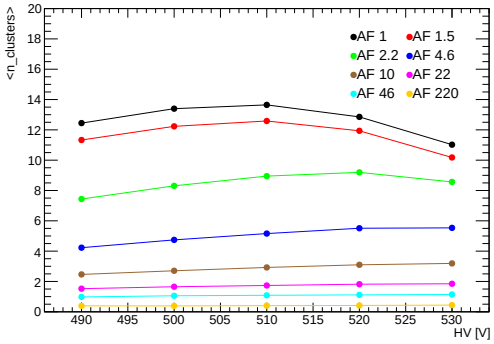

(d) Mean number of clusters versus high voltage at 9 mV/fC gain.

Figure 7.8: Comparison of mean raw hits and mean number of clusters as a function of high voltage between 1 mV/fC and 9 mV/fC gain.

FELIX team created a new firmware introducing a variety of different delays[3]. The new firmware was tested extensively, using the parameters that were under evaluation in the previous testbeam periods. In the following plots can be observed the relationship between mean number of clusters with the gamma intensity for the varying delays (figures 7.9 and 7.10) at 520 V. One can easily infer that the plots with delay (new firmware) do not show any significant difference compared to the case of no delay. Upon closer examination, the former exhibit a lower number of clusters compared to the latter case. In conclusion, it can be assumed that the the data loss is not correlated to the timing of L0A and L1A signals.

[3]The delay introduced is of the order of several Bunch Crossings (BC), where one BC equals 25 ns.

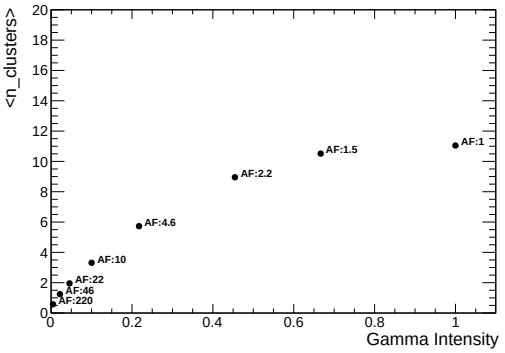

(a) Mean number of clusters versus gamma intensity at 520 V, with 16 BCs delay.

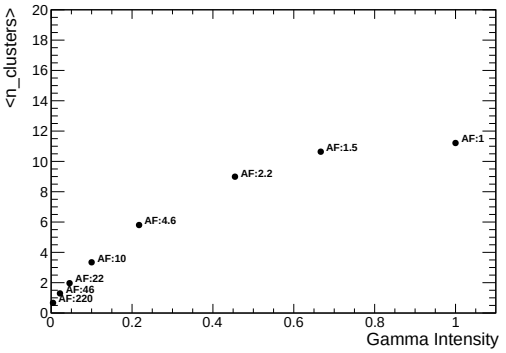

(b) Mean number of clusters versus gamma intensity at 520 V, with 63 BCs delay.

Figure 7.9: Comparison of mean number of clusters as a function of gamma intensity with the two different delays between L0A and L1A signals.

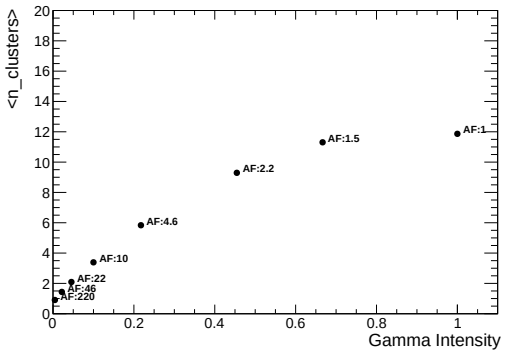

Figure 7.10: Mean number of clusters versus gamma intensity at 520 V, with no delay.

7.4.1 SLH REGISTER

A few more failed attempts followed until the encounter of a register in the VMM ASIC, known as slh [52]. The slh register, forces a faster restoration of the baseline[4], by increasing the bias current at input node, from nominal value of 1 nA to 15 nA. Its values are either 0 or 1 (on/off). In simple terms, when the charge accumulated by a strip, enters the low-noise charge amplifier[5] (of a VMM channel) the integration starts in order to produce the output voltage.

[4] The term baseline refers to a stable reference or initial state, against which changes or variations in a signal are measured.

[5] The primary function of a charge amplifier is to integrate the input charge over time and convert it into a voltage.

When increasing the bias current at input node, the charge amplifier becomes more sensitive to incoming charges, since the bias current sets the initial operational conditions for the amplifier and plays a crucial role, in how quickly the amplifier can respond to changes in the input charge. Thus, it can integrate the accumulated charge more quickly and bring the output closer to the expected value. Moreover, the integration time of a charge amplifier can be reduced, by increasing the input bias current, since it is inversely proportional to it. Consequently, it can effectively "speed up" the integration process, helping the amplifier reach the correct output voltage faster.

The tests continued accumulating data with the slh register on (value 1), employing the usual parameters. The results can be found on the right side of the page (fig. 7.12). The plots illustrate the mean raw hits, mean number of clusters and the mean hit occupancy as a function of gamma intensity at 530 V, with a peaking time of 200 ns, for slh values of 0 and 1. The difference between using the register (slh = 1) and not using it (slh = 0), is quite pronounced. As one can observe, there is a clear improvement on the data loss. Taking the plot 7.12b as an example, the number of clusters with slh = 0 at attenuation factor 1 is approximately 11 whereas for the case of slh 1 is approximately 16. Furthermore, it is observed that the linear behaviour is restored up to attenuation factor of 1.5, with the saturation effect being evident only at attenuation factor of 1.

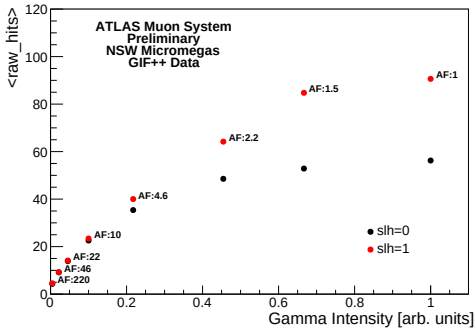

(a) Raw hits of clusters versus gamma intensity at 530 V

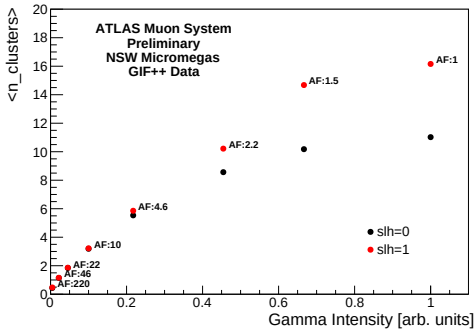

(b) Mean number of clusters versus gamma intensity at 530 V

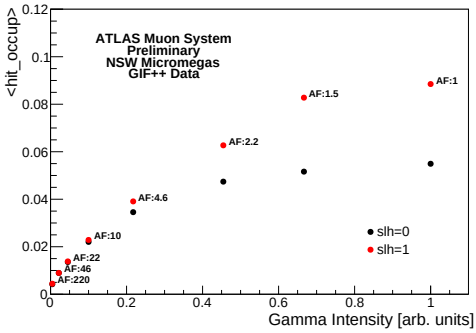

(c) Hit occupancy of clusters versus gamma intensity at 530 V

Figure 7.11: Comparison plots of slh = 0 and 1.

Data have also been collected with a peaking time of 100 ns, in order to observe the impact of the shorter integration time. The following graphs depict the mean raw hits, mean number of clusters and the mean hit occupancy as a function of gamma intensity at 530 V, with slh = 1, considering the two different peaking time values. It is quite

obvious that the outcome is even better for the case of 100 ns peaking time, giving the ability to retrieve even more data.

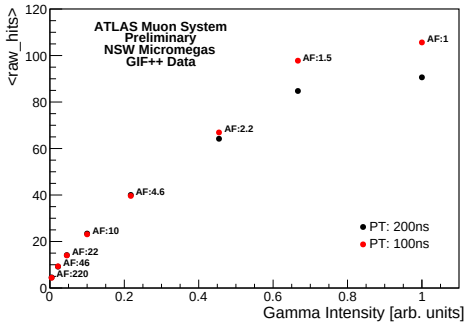

(a) Raw hits of clusters versus gamma intensity at 530 V

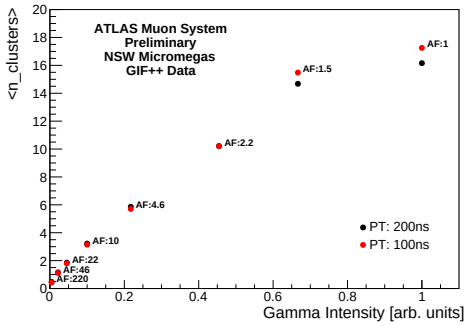

(b) Mean number of clusters versus gamma intensity at 530 V

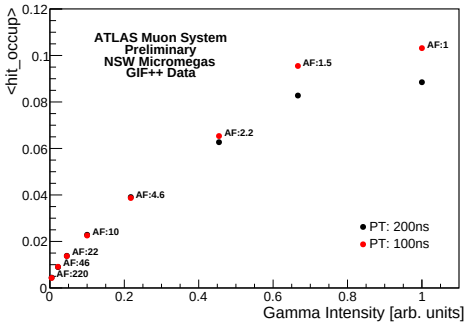

(c) Hit occupancy of clusters versus gamma intensity at 530 V

Figure 7.12: Comparison plots of 100 ns and 200 ns peaking time, with slh = 1.

Based on the studies that have been performed and the plots that have been presented, it is reasonable to assume that the primary cause of data loss, at a first level, is attributed to the high gamma ray activity, in the detector and consequently to the VMM ASIC. More specifically, the VMM is affected because it has to process a substantial amount of charge (especially at low attenuation factors) that the integration performed by the charge amplifier takes an extended amount of time (with slh register off). This, in turn, results in significant dead times and consequently leads to data loss.

Furthermore, at a secondary level, the 10bit ADC (1024 channels), appears to contribute to data loss as it imposes an upper limit on the charge it can process, leading to the saturation effect. This contribution can be inferred from the charge distribution of a given run. In figure 7.13 can be found the charge distribution at 520 V, 9 mV/fC gain, slh 0, for attenuation factors 1 and 220, which were used for completeness. Focusing on the right part of the plots, one can observe a peak, which can be explained only by the fact that the 10-bit ADC is not sufficient to store entries beyond the 1024th channel. Consequently, those entries are added to the 1024th channel. Ideally, it would be expected to have very few entries near the last channels of the 10-bit ADC.

However, it has been proven that using the slh register (value 1) results in considerable less data loss. Furthermore, it is worth mentioning that the use of slh register has already been deployed in the configuration of VMM ASICs used in MM detector in the ATLAS cavern. Additionally, it is important to emphasize that both detector technologies in NSW, MM and sTGC, en-

counter background activity equivalent to that of attenuation factor 10. This is far from the rates of attenuation factors 1 and 1.5, which exhibit digression due to saturation.

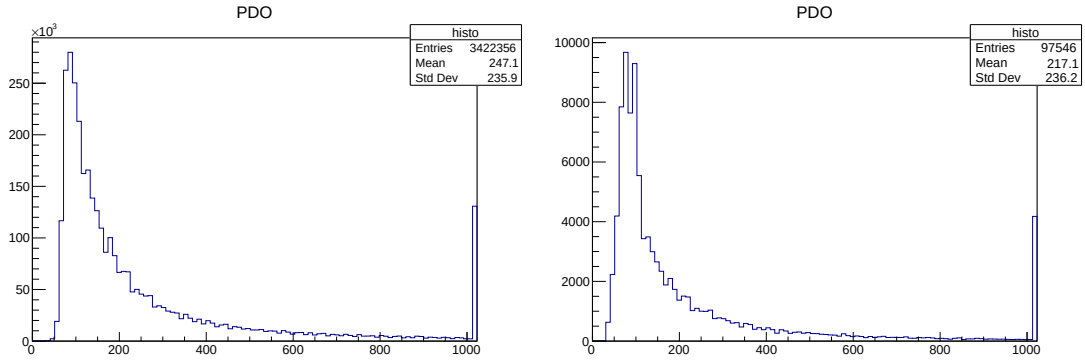

(a) Charge distribution at 520 V, 9 mV/fC gain, slh 0 and attenuation factor 1.

(b) Charge distribution at 520 V, 9 mV/fC gain, slh 0 and attenuation factor 220.

Figure 7.13: Comparison of charge distributions at attenuation factor 1 and 220.

8 Summary

In this chapter, the work carried out throughout this master's thesis is summarised, and the future directions for this research are outlined. The objective of this thesis was the development of NSW Detector Control System (DCS) and the performance study of Micromegas detectors under high radiation environment.

The recent integration of NSWs into ATLAS detector, made the development of a new control system mandatory, as all detectors require a corresponding system able to control and monitor their parameters. This thesis, focused on the further development of NSW DCS in order to cover the emerging needs of detector experts. The updates that were implemented were on the user interface, with the addition of advanced/expert panels and on the low-level of the system, with parts of existing code re-written in a more efficient way. In more detail, python scripts and tools have been created, managing XML and JSON files in order to allow the enabling or disabling of boards within the FSM. Another issue addressed with the optimisation of existing scripts, was the FSM freezing during low voltage changes. Although the core features of NSW DCS have been finalised and the majority of bugs have been addressed, the operation of detectors is a dynamical system that changes creating new needs.

One of the detector technologies housed in NSWs is the Micromegas, a gaseous detector that is mainly deployed for precision tracking, given its high spatial resolution. The second part of the present thesis was the assessment of resistive Micromegas detectors under high radiation environment. This assessment aimed to confirm that Micromegas modules can perform equally efficiently after having been exposed to irradiation equivalent to about 10 years in the High-Luminosity LHC (HL-LHC) environment. The tests were performed in two different testbeam periods, in July and October 2022. The testbeam in July, focused on the SM1 module, collecting valuable data for various experimental parameters, such as high voltage, attenuation factor, VMM threshold, peaking time, and gain. In the October testbeam, LM2 module was added to the detectors under testing. The investigation revealed an unexpected data loss issue in October's testbeam data. After extensive investigation, it was found that enabling the slh register in the VMM ASIC, which increases the bias current at the input node, the data loss was significantly reduced in high gamma intensity (or low attenuation factor). As a result of the investigation the slh parameter has also been enabled on the configuration files of Point 1 (ATLAS experiment).

Looking ahead, a thorough analysis of the impact of the slh register in data taking must be conducted based on the data from the July 2023 testbeam period. During this testbeam period, the parameters under investigation remained the same as in the previous testbeams, with the addition of the slh register. Furthermore, an evaluation of the efficiency and resolution uniformity will be conducted next summer on the SM1 module in the H8C line, with the aim of validating its seamless performance after the prolonged exposure to radiation.

Acronyms

ADDC	ART Data Driver Card
ALICE	A Large Ion Collider Experiment
ASIC	Application-Specific Integrated Circuit
ATLAS	A Toroidal LHC ApparatuS
BC	Bunch Crossing
CERN	Conseil Européen pour la Recherche Nucléaire
CMS	Compact Muon Solenoid
CSC	Cathode Strip Chambers
DCS	Detector Control System
FELIX	Front-End LInk eXchange
FPGA	Field Programmable Gate Array
FSM	Finite State Machine
GBLD	Gigabit Laser Driver
GBT	Giga-Bit Transiver
GBTIA	GigaBit Transimpedance Amplifier
HL-LHC	High-Luminosity LHC
HLT	High-Level Trigger
ID	Inner Detector
JCOP	Joint COntrols Project
L1	Level-1
L1DDC	Level-1 Data Driver Card
LAr	Liquid Argon
LEIR	Low Energy Ion Ring
LHC	Large Hadron Collider
LHCb	Large Hadron Collider beauty
MDT	Monitored Drift Tubes
MM	Micromegas
MMFE8	MicroMegas Front-End 8
MWPC	Multi-Wire Proportional Chamber
NSW	New Small Wheel
PCB	Printed Circuit Board
PS	Proton Synchrotron
PSB	Proton Synchrotron Booster
ROC	Read-Out Controller
ROI	Region of Interest

RPC	Resistive Plate Chambers
SCA	Slow Control Adapter
SCADA	Supervisory Control and Data Acquisition
SCT	Semiconductor Tracker
SPS	Super Proton Synchrotron
sTGC	small-strip Thin Gap Chambers
TDAQ	Trigger and Data Acquisition
TGC	Thin Gap Chambers
TRT	Transition Radiation Tracker
VMM	Versatile Readout Module
VTRx	Versatile Transceiver
XML	Extensible Markup Language

Bibliography

1. M. Krause. *CERN How We Found the HIGGS BOSON*. World Scientific, Singapore, 2014.
2. L. Arnaudon et al. *Linac4 Technical Design Report*. Technical report. revised version submitted on 2006-12-14 09:00:40. Geneva: CERN, 2006. URL: https://cds.cern.ch/record/1004186.
3. P. Gagnon. *WHO CARES ABOUT PARTICLE PHYSICS?* Oxford university press, United Kingdom, 2016.
4. O. S. Brüning, P. Collier, P. Lebrun, S. Myers, R. Ostojic, J. Poole, and P. Proudlock. *LHC Design Report*. CERN Yellow Reports: Monographs. CERN, Geneva, 2004. DOI: 10.5170/CERN-2004-003-V-1. URL: https://cds.cern.ch/record/782076.
5. D. Brandt, ed. *CERN Accelerator School Intermediate accelerator physics*. CERN, Geneva, 2006, pp. 361–377. URL: http://cds.cern.ch/record/603056.
6. T. A. Collaboration. *The ATLAS Experiment at the CERN Large Hadron Collider*. Nuclear JINST 3 S08003, 2008.
7. *ATLAS inner detector: Technical Design Report, 1*. Technical design report. ATLAS. CERN, Geneva, 1997. URL: https://cds.cern.ch/record/331063.
8. *ATLAS magnet system: Technical Design Report, 1*. Technical design report. ATLAS. CERN, Geneva, 1997. DOI: 10.17181/CERN.9O5C.VDTM. URL: https://cds.cern.ch/record/338080.
9. *ATLAS liquid-argon calorimeter: Technical Design Report*. Technical design report. ATLAS. CERN, Geneva, 1996. DOI: 10.17181/CERN.FWRW.FOOQ. URL: https://cds.cern.ch/record/331061.
10. *ATLAS tile calorimeter: Technical Design Report*. Technical design report. ATLAS. CERN, Geneva, 1996. DOI: 10.17181/CERN.JRBJ.7O28. URL: https://cds.cern.ch/record/331062.
11. *ATLAS muon spectrometer: Technical Design Report*. Technical design report. ATLAS. CERN, Geneva, 1997. URL: https://cds.cern.ch/record/331068.
12. G. Aad et al. *Technical Design Report for the Phase-I Upgrade of the ATLAS TDAQ System*. Technical report. Final version presented to December 2013 LHCC. 2013. URL: https://cds.cern.ch/record/1602235.

13. A. Poy, H. Boterenbrood, H. Burckhart, J. Cook, V. Filimonov, S. Franz, O. Gutzwiller, B. Hallgren, V. Khomutnikov, S. Schlenker, and F. Varela Rodriguez. "The detector control system of the ATLAS experiment". *Journal of Instrumentation - J INSTRUM* 3, 2008. DOI: 10.1088/1748-0221/3/05/P05006.

14. O. Aberle et al. *High-Luminosity Large Hadron Collider (HL-LHC): Technical design report*. CERN Yellow Reports: Monographs. CERN, Geneva, 2020. DOI: 10.23731/CYRM-2020-0010. URL: https://cds.cern.ch/record/2749422.

15. T. Kawamoto, S. Vlachos, L. Pontecorvo, J. Dubbert, G. Mikenberg, P. Iengo, C. Dallapiccola, C. Amelung, L. Levinson, R. Richter, and D. Lellouch. *New Small Wheel Technical Design Report*. Technical report. ATLAS New Small Wheel Technical Design Report. 2013. URL: https://cds.cern.ch/record/1552862.

16. G. Charpak, R. Bouclier, T. Bressani, J. Favier, and Č. Zupančič. "The use of multiwire proportional counters to select and localize charged particles". *Nuclear Instruments and Methods* 62:3, 1968, pp. 262–268. ISSN: 0029-554X. DOI: https://doi.org/10.1016/0029-554X(68)90371-6. URL: https://www.sciencedirect.com/science/article/pii/0029554X68903716.

17. Y. Giomataris, P. Rebourgeard, J. Robert, and G. Charpak. "MICROMEGAS: a high-granularity position-sensitive gaseous detector for high particle-flux environments". *Nuclear Instruments and Methods in Physics Research Section A: Accelerators, Spectrometers, Detectors and Associated Equipment* 376:1, 1996, pp. 29–35. ISSN: 0168-9002. DOI: https://doi.org/10.1016/0168-9002(96)00175-1. URL: https://www.sciencedirect.com/science/article/pii/0168900296001751.

18. T. Alexopoulos et al. "Development of large size Micromegas detector for the upgrade of the ATLAS Muon system". *Nuclear Instruments and Methods in Physics Research Section A: Accelerators, Spectrometers, Detectors and Associated Equipment* 617:1, 2010. 11th Pisa Meeting on Advanced Detectors, pp. 161–165. ISSN: 0168-9002. DOI: https://doi.org/10.1016/j.nima.2009.06.113. URL: https://www.sciencedirect.com/science/article/pii/S0168900209013485.

19. G. Aad et al. *Technical Design Report for the Phase-I Upgrade of the ATLAS TDAQ System*. Technical report. Final version presented to December 2013 LHCC. 2013. URL: https://cds.cern.ch/record/1602235.

20. P. Gkountoumis. *Electronics Design and System Integration of the ATLAS New Small Wheels*. Technical report. Geneva: CERN, 2016. URL: https://cds.cern.ch/record/2235777.

21. G. Iakovidis, V. Polychronakos, and G. De Geronimo. *VMM - An ASIC for micropattern detectors*. Technical report. Geneva: CERN, 2015. DOI: 10.1051/epjconf/201817407001. URL: https://cds.cern.ch/record/2104297.

22. A. Caratelli, S. Bonacini, K. Kloukinas, A. Marchioro, P. Moreira, R. De Oliveira, and C. Paillard. "The GBT-SCA, a radiation tolerant ASIC for detector control and monitoring applications in HEP experiments". *JINST* 10:03, 2015, p. C03034. DOI: 10.1088/1748-0221/10/03/C03034. URL: https://cds.cern.ch/record/2158969.

23. R.-M. Coliban, S. Popa, T. Tulbure, D. Nicula, M. Ivanovici, S. Martoiu, L. Levinson, and J. Vermeulen. "The Read Out Controller for the ATLAS New Small Wheel". *Journal of Instrumentation* 11:02, 2016, p. C02069. DOI: 10.1088/1748-0221/11/02/C02069. URL: https://dx.doi.org/10.1088/1748-0221/11/02/C02069.

24. P. Gkountoumis and T. Alexopoulos. "Design and development of the Level-1 Data Driver Card (L1DDC) for the New Small Wheel upgrade of the ATLAS experiment at CERN". Presented 08 Apr 2019. PhD thesis. National Technical University of Athens, 2019. URL: http://cds.cern.ch/record/2674048.

25. K. T. Bauer. *FELIX: the new detector readout system for the ATLAS experiment*. Technical report. Geneva: CERN, 2017. URL: https://cds.cern.ch/record/2292375.

26. P. Moreira, R. Ballabriga, S. Baron, S. Bonacini, O. Cobanoglu, F. Faccio, T. Fedorov, R. Francisco, P. Gui, P. Hartin, K. Kloukinas, X. Llopart, A. Marchioro, C. Paillard, N. Pinilla, K. Wyllie, and B. Yu. "The GBT Project", 2009. DOI: 10.5170/CERN-2009-006.342. URL: https://cds.cern.ch/record/1235836.

27. J. Troska, V. Bobillier, S. Detraz, S. Papadopoulos, I. Papakonstantinou, S. Storey, C. Sigaud, P. Stejskal, C. Soos, and F. Vasey. "Versatile Transceiver developments". *Journal of Instrumentation* 6:01, 2011, p. C01089. DOI: 10.1088/1748-0221/6/01/C01089. URL: https://dx.doi.org/10.1088/1748-0221/6/01/C01089.

28. L. Yao, V. Polychronakos, H. Chen, K. Chen, H. Xu, S. Martoiu, N. Felt, and T. Lazovich. "The address in real time data driver card for the MicroMegas detector of the ATLAS muon upgrade". *JINST* 12:01, 2017, p. C01047. DOI: 10.1088/1748-0221/12/01/C01047. URL: https://cds.cern.ch/record/2291325.

29. S. Schlenker et al. "The ATLAS Detector Control System". *Conf. Proc.* C111010, 2011, MOBAUST02. URL: https://cds.cern.ch/record/1562594.

30. O. Holme, M. Gonzalez-Berges, P. Golonka, and S. Schmeling. "The JCOP framework". *Conf. Proc. C051010:WE* 2, 2005.

31. H. Boterenbrood, H. Burckhart, J. Cook, V. Filimonov, B. Hallgren, W. Heubers, V. Khomutnikov, Y. Ryabov, and F. Varela Rodriguez. "Design and implementation of the ATLAS detector control system". *Nuclear Science, IEEE Transactions on* 51, 2004, pp. 495–501. DOI: 10.1109/TNS.2004.828523.

32. P. P. Nikiel, B. Farnham, S. Franz, S. Schlenker, H. Boterenbrood, and V. Filimonov. "OPC Unified Architecture within the Control System of the ATLAS Experiment", 2014. URL: https://cds.cern.ch/record/1696973.

33. Siemens. *SIMATIC WinCC Open Architecture Version 3.19*. 2023. URL: https://www.winccoa.com/documentation/WinCCOA/latest/en_US/GettingStarted/GettingStarted-06.html?hl=architecture (visited on 06/15/2023).

34. P. Tzanis. "The Detector Control System of the New Small Wheel for the ATLAS experiment". *Journal of Physics: Conference Series* 2105:1, 2021, p. 012025. DOI: 10.1088/1742-6596/2105/1/012025. URL: https://dx.doi.org/10.1088/1742-6596/2105/1/012025.

35. P. P. Nikiel, B. Farnham, V. Filimonov, and S. Schlenker. "Generic OPC UA Server Framework". *Journal of Physics: Conference Series* 664:8, 2015, p. 082039. DOI: 10.1088/1742-6596/664/8/082039. URL: https://dx.doi.org/10.1088/1742-6596/664/8/082039.

36. P. Tzanis. *NswXmlGenerator*. 2022. URL: https://gitlab.cern.ch/ptzanis/nswxmlgenerator (visited on 08/23/2023).

37. Siemens. *Mapping (associative arrays)*. 2023. URL: https://www.winccoa.com/documentation/WinCCOA/latest/en_US/Control_Grundlagen/Control_Grundlagen-38.html?hl=mapping (visited on 09/01/2023).

38. P. Nikiel, P. Moschovakos, and B. Farnham. *Cacophony*. 2019. URL: https://github.com/quasar-team/Cacophony (visited on 08/31/2023).

39. P. Moschovakos. *OpcUaSca*. 2020. URL: https://gitlab.cern.ch/atlas-dcs-opcua-servers/ScaOpcUa (visited on 08/31/2023).

40. R. Alemany, M. Lamont, and S. Page. "LHC modes", 2007.

41. H. Kolanoski and N. Wermes. "1Introduction". In: *Particle Detectors: Fundamentals and Applications*. Oxford University Press, 2020. ISBN: 9780198858362. DOI: 10.1093/oso/9780198858362.003.0001. eprint: https://academic.oup.com/book/0/chapter/365027446/chapter-pdf/50270332/oso-9780198858362-chapter-1.pdf. URL: https://doi.org/10.1093/oso/9780198858362.003.0001.

42. M. Tanabashi et al. "Review of Particle Physics". *Phys. Rev. D* 98, 3 2018, p. 030001. DOI: 10.1103/PhysRevD.98.030001. URL: https://link.aps.org/doi/10.1103/PhysRevD.98.030001.

43. G. F. Knoll. *Radiation Detection and Measurement, 3rd ed.* 3rd edition. John Wiley and Sons, New York, 2000. ISBN: 978-0-471-07338-3, 978-0-471-07338-3.

44. F. Sauli. *Gaseous Radiation Detectors, Fundamentals and Applications*. 3rd edition. Cambridge University Press, United Kingdom, 2015. ISBN: 978-1-009-29118-7, 978-1-009-29121-7.

45. J. S. T. M.A. "XVII. The Conductivity produced in gases by the motion of negatively charged ions". *The London, Edinburgh, and Dublin Philosophical Magazine and Journal of Science* 1:2, 1901, pp. 198–227. DOI: 10.1080/14786440109462605. eprint: https://doi.org/10.1080/14786440109462605. URL: https://doi.org/10.1080/14786440109462605.

46. W. Shockley. "Currents to conductors induced by a moving point charge". *J. Appl. Phys.* 9:10, 1938, pp. 635–636. DOI: 10.1063/1.1710367.

47. S. Ramo. "Currents induced by electron motion". *Proc. Ire.* 27, 1939, pp. 584–585. DOI: 10.1109/JRPROC.1939.228757.

48. M. Dris and T. Alexopoulos. *Signal Formation in Various Detectors*. 2017. arXiv: 1406.3217 [hep-ex].

49. M. R. Jakel, M. Capeans, I. Efthymiopoulos, A. Fabich, A. Guida, G. Maire, M. Moll, D. Pfeiffer, F. Ravotti, and H. Reithler. "CERN GIF++ : A new irradiation facility to test large-area particle detectors for the high-luminosity LHC program". *PoS* TIPP2014, 2014, p. 102. URL: https://cds.cern.ch/record/1977147.

50. D. Pfeiffer, G. Gorine, H. Reithler, B. Biskup, A. Day, A. Fabich, J. Germa, R. Guida, M. Jaekel, and F. Ravotti. "The radiation field in the Gamma Irradiation Facility GIF++ at CERN". *Nuclear Instruments and Methods in Physics Research Section A: Accelerators, Spectrometers, Detectors and Associated Equipment* 866, 2017, pp. 91–103. ISSN: 0168-9002. DOI: https://doi.org/10.1016/j.nima.2017.05.045. URL: https://www.sciencedirect.com/science/article/pii/S0168900217306113.

51. P. Lösel and R. Müller. *Design and Construction of Large Size Micromegas Chambers for the Upgrade of the ATLAS Muon Spectrometer*. Technical report. 2015. arXiv: 1508.02541. URL: https://cds.cern.ch/record/2042404.

52. *The VMM3a User's Guide*. Technical report. All figures including auxiliary figures are available at https://atlas.web.cern.ch/Atlas/GROUPS/PHYSICS/PUBNOTES/ATL-MUON-PUB-2022-002. Geneva: CERN, 2022. URL: https://cds.cern.ch/record/2807691.